Deletion of *Serf2* shifts amyloid conformation in an Aβ amyloid mouse model

E. Stroo[1*], L. Janssen[1*], O. Sin[1], W. Hogewerf[1], M. Koster[2], L. Harkema[2], S.A. Youssef[2,3], N. Beschorner[4], A.H.G. Wolters[5], B. Bakker[1], A. Thathiah[6,7], F. Foijer[1], B. van de Sluis[2], J. van Deursen[8], M. Jucker[4], A. de Bruin[2,3], E.A.A. Nollen[1]

[1]European Research Institute for the Biology of Ageing, University of Groningen, University Medical Centre Groningen, The Netherlands

[2]Department of Biomolecular Health Sciences, Faculty of Veterinary Medicine, Utrecht University, The Netherlands

[3]Department of Pediatrics, Molecular Genetics Section, University of Groningen, University Medical Centre Groningen, The Netherlands

[4]Department of Cellular Neurology, Hertie-Institute for Clinical Brain Research, University of Tübingen, Tübingen, Germany.

[5]Department of Biomedical Sciences of Cells and Systems, University Medical Centre Groningen, The Netherlands

[6]VIB Center for the Biology of Disease, KU Leuven Center for Human Genetics, University of Leuven, Leuven, Belgium

[7] Department of Neurobiology, University of Pittsburgh Brain Institute, University of Pittsburgh School of Medicine, Pittsburgh, PA USA

[8]Mayo Clinic, United States of America

*These authors contributed equally

[#]Correspondence: e.a.a.nollen@umcg.nl

Keywords: Small EDRK-rich factor 2, SERF, protein aggregation, amyloid-beta, amyloid polymorphisms

25 **Highlights**

26 - Loss of SERF2 slows embryonic development and causes perinatal lethality
27 - SERF2 affects proliferation in a cell-autonomous fashion
28 - Brain-specific *Serf2* knockout does not affect viability or Aβ production
29 - Brain deletion of *Serf2* shifts the amyloid conformation of Aβ

Abstract

Neurodegenerative diseases like Alzheimer, Parkinson and Huntington disease are characterized by aggregation-prone proteins that form amyloid fibrils through a nucleation process. Despite the shared β-sheet structure, recent research has shown that structurally different polymorphs exist within fibrils of the same protein. These polymorphs are associated with varying levels of toxicity and different disease phenotypes. MOAG-4 and its human orthologs SERF1 and SERF2 have previously been shown to modify the nucleation and drive amyloid formation and protein toxicity *in vitro* and in *C. elegans*. To further explore these findings, we generated a *Serf2* knockout (KO) mouse model and crossed it with the *APPPS1* mouse model for Aβ amyloid pathology. Full-body KO of *Serf2* resulted in a developmental delay and perinatal lethality due to insufficient lung maturation. Therefore, we proceeded with a brain-specific *Serf2* KO, which was found to be viable. We examined the Aβ pathology at 1 and 3 months of age, which is before and after the start of amyloid deposition. We show that SERF2 deficiency does not affect the production and overall Aβ levels. *Serf2* KO-*APPPS1* mice displayed an increased intracellular Aβ accumulation at 1 month and a higher number of Aβ deposits compared to *APPPS1* mice with similar Aβ levels. Moreover, conformation-specific dyes and electron microscopy revealed a difference in the structure and amyloid content of these Aβ deposits. Together, our results reveal that SERF2 causes a structural shift in Aβ aggregation in a mammalian brain. These findings indicate that a single endogenous factor may contribute to amyloid polymorphisms, allowing for new insights into this phenomenon's contribution to disease manifestation.

50 **Introduction**

51 Protein aggregation is a pathological hallmark shared by several age-related neurodegenerative
52 diseases, such as Alzheimer (AD), Parkinson and Huntington disease. The amyloid-like aggregates
53 that accumulate in each of these diseases are composed of disease-specific proteins, i.e., amyloid-beta
54 (Aβ) and tau in AD(Glenner & Wong, 1984; Masters *et al*, 1985; Grundke-Iqbal *et al*, 1986a, 1986b),
55 alpha-synuclein (α-Syn) in Parkinson disease(Langley & Charlesworth, 1997) and Huntingtin (HTT)
56 in Huntington disease(Scherzinger *et al*, 1999). While the exact molecular mechanisms underlying the
57 disease pathology remain to be elucidated, genetic evidence indicates that these aggregation-prone
58 proteins play a key role in the disease processes. In AD multiple causative mutations have been found
59 in three genes: the amyloid precursor protein (*APP*)(Goate *et al*, 1991; Chartier-Harlin *et al*, 1991;
60 Citron *et al*, 1992; Eckman *et al*, 1997; Murrell *et al*, 2000; Kumar-Singh *et al*, 2000; Cruts *et al*,
61 2003; Kumar-Singh *et al*, 2006; Tomiyama *et al*, 2008), presenilin-1 (*PSEN1*)(Schellenberg *et al*,
62 1992; Sherrington *et al*, 1995; Borchelt *et al*, 1996; Lemere *et al*, 1996; Guerreiro *et al*, 2010) and
63 presenilin-2 (*PSEN2*)(Rogaev *et al*, 1995; Citron *et al*, 1997; Müller *et al*, 2014; Guerreiro *et al*, 2010)
64 (for a full list of known AD-linked mutations see https://www.alzforum.org/mutations). The *APP*
65 gene encodes the precursor protein from which Aβ is produced through sequential cleavage by a β-
66 and γ-secretase. The *PSEN* genes encode the main catalytic subunit of the γ-secretase complex. The
67 fact that all the causative mutations affect the production, length and/or structure of the Aβ peptides
68 and are sufficient to cause the disease(Chartier-Harlin *et al*, 1991; Citron *et al*, 1997; Cruts *et al*, 2003;
69 Eckman *et al*, 1997; Guerreiro *et al*, 2010; Goate *et al*, 1991; Kumar-Singh *et al*, 2000, 2006; Lemere
70 *et al*, 1996; Müller *et al*, 2014; Murrell *et al*, 2000; Rogaev *et al*, 1995; Schellenberg *et al*, 1992;
71 Sherrington *et al*, 1995; Tomiyama *et al*, 2008; Borchelt *et al*, 1996; Citron *et al*, 1992), is arguably
72 the strongest piece of evidence for the involvement of Aβ in the disease process. Causative mutations
73 generally affect the Aβ peptide in one of three ways: (i) an overall increase in Aβ production(Haass *et*
74 *al*, 1995; Citron *et al*, 1992), (ii) a shift in the production of shorter variants, like $A\beta_{40,}$ to more
75 aggregation-prone, longer variants, like $A\beta_{42}$ (or $A\beta_{43}$)(Suzuki *et al*, 1994; Duff *et al*, 1996; Murayama
76 *et al*, 1999; Murrell *et al*, 2000; Borchelt *et al*, 1996), (iii) Aβ peptides with a modified core region,

77 resulting in an increased propensity for aggregation(Nilsberth *et al*, 2001; Miravalle *et al*, 2000; Ni *et*
78 *al*, 2011; Tomiyama *et al*, 2008). Taken together, these mutations do not necessarily increase the
79 amount of Aβ, but rather increase the likelihood of Aβ aggregation. Similarly, several mutations
80 in the *SNCA* gene that have been linked to Parkinson disease have been shown to alter α-Syn
81 aggregation(Conway *et al*, 1998; Narhi *et al*, 1999; Conway *et al*, 2000; Ghosh *et al*, 2013, 2014; Choi
82 *et al*, 2004). In Huntington disease, any expansion of a polyglutamine stretch in the *HTT* gene that
83 exceeds 36 repeats has been shown to facilitate HTT aggregation and cause the disease(Cooper *et al*,
84 1998). Hence, changes in the folding and aggregation of these disease proteins are believed to be at the
85 basis of the observed pathology. In addition, there is increasing evidence that distinct structural
86 variants exist between aggregates of the same disease protein and that these polymorphs are associated
87 with varying degrees of toxicity(Nekooki-Machida *et al*, 2009; Sun *et al*, 2015; Cohen *et al*, 2015;
88 Qiang *et al*, 2017; Bousset *et al*, 2013; Heise *et al*, 2008; Li *et al*, 2018; Guerrero-Ferreira *et al*, 2019;
89 Gath *et al*, 2014; Cohen *et al*, 2009) . For instance, recent studies with brain samples from human AD
90 patients have shown that variations in the disease type and disease progression correlate with the
91 presence of structurally different aggregates and fibrils(Lu *et al*, 2013; Rasmussen *et al*, 2017; Cohen
92 *et al*, 2015; Qiang *et al*, 2017). The knowledge that small changes in the structural conformation of
93 these aggregates can have far-reaching effects on the disease manifestation could provide a new
94 avenue for the development of therapeutics. Until now, most research into potential treatments of AD
95 has focused on either reducing the overall amount of aggregating proteins or preventing aggregation,
96 not modifying the aggregation process.

97 In a previous study, our group performed a genetic screen in *Caenorhabditis elegans* (*C. elegans*) and
98 identified a small, intrinsically disordered protein of unknown function with the capacity to modify
99 protein aggregation and to enhance the resulting toxicity of multiple disease-related, aggregation-
100 prone proteins(van Ham *et al*, 2010). This peptide was dubbed *mo*difier of *ag*gregation-4 (MOAG-4)
101 and was found to be an ortholog of two human genes: *Serf1A* and *Serf2*. Both SERF1A and SERF2
102 were shown to exacerbate protein aggregation and toxicity in human neuroblastoma and HEK293 cell
103 lines as well(van Ham *et al*, 2010). *In vitro* assays with MOAG-4 and SERF1A have demonstrated

104 that these proteins can specifically accelerate the aggregation kinetics of amyloidogenic proteins, but
105 do not affect aggregation of non-amyloidogenic proteins(Falsone *et al*, 2012; Yoshimura *et al*, 2017).
106 For α-Syn, this amyloid-promoting effect has been shown to depend on the transient interaction of
107 these positively-charged peptides with negatively-charged regions and the disruption intramolecular
108 electrostatic interactions within the protein(Merle *et al*, 2019; Falsone *et al*, 2012; Yoshimura *et al*,
109 2017). Removal of MOAG-4 or SERF from a biological system did not change the overall levels of
110 the aggregation-prone proteins or activate chaperone pathways known to suppress aggregation(van
111 Ham *et al*, 2010). Therefore, the reduced toxicity would appear to rely solely on the structural shift in
112 the aggregation process(van Ham *et al*, 2010; Falsone *et al*, 2012). In this study, we investigate
113 whether the removal of SERF2 modifies the aggregation of Aβ in the biologically more complex
114 environment of the mammalian brain.

115 **Results**

116 *Full-body Serf2 KO results in developmental delay and perinatal lethality in mice*

117 To establish the role of SERF2 *in vivo*, full-body *Serf2* knockout (KO) mice were generated (Figure
118 S1A-C). During an initial cross, using the four homozygous *Serf2* KO animal (*Serf2*$^{-/-}$) and eight
119 heterozygous *Serf2* KO animals (*Serf2*$^{+/-}$) we obtained, only one *Serf2*$^{-/-}$ survived the day of birth
120 compared to 27 *Serf2*$^{+/-}$ and 96 *Serf2* wild-type (*Serf2*$^{+/+}$) mice (Supplemental Table 1). After
121 backcrossing into C57BL/6J background, interbreeding of *Serf2*$^{+/-}$ animals did not result in any viable
122 *Serf2*$^{-/-}$ mice at the time of weaning (Figure 1A,1B). To determine whether *Serf2*$^{-/-}$ mice died during
123 fetal development, we examined the offspring at multiple developmental stages: embryonic day 13.5,
124 15.5 and 17.5. In all of the examined embryonic stages we observed the expected Mendelian ratio of
125 genotypes, around 25 % *Serf2*$^{+/+}$ and *Serf2*$^{-/-}$ embryos and around 50 % *Serf2*$^{+/-}$ (Chi Square: E13.5
126 p=0.9672; E15.5 p= 0.4432; E17.5 p=0.7674) (Figure 1B). At birth (P0), all *Serf2*$^{-/-}$ displayed
127 respiratory distress and the majority (5/7) died within 30 minutes of being born. At the time of
128 weaning, the Mendelian ratio was maintained between the *Serf2*$^{+/+}$ and *Serf2*$^{+/-}$ animals, but no *Serf2*$^{-/-}$
129 mice survived until this stage (Chi Square: P22 p<0.0001) . Examination of *Serf2* mRNA expression at
130 E13.5 showed a 50 % reduction for *Serf2*$^{+/-}$ and complete KO for *Serf2*$^{-/-}$ compared to *Serf2*$^{+/+}$ (One-
131 way ANOVA: *Serf2*$^{+/-}$ and *Serf2*$^{-/-}$ vs *Serf2*$^{+/+}$ p_{Bon}<0.0001) (Figure 1C). A similar ratio in SERF2
132 expression was also observed on the protein level (Figure 1D). The *Serf1* mRNA levels were not
133 affected by the change in *Serf2* levels, indicating there is no compensatory mechanism between these
134 genes (One-way ANOVA: p=0.2403) (Figure 1C). Further analysis of the *Serf2*$^{-/-}$ embryonic
135 phenotype revealed a reduction in embryo size of *Serf2*$^{-/-}$ compared to *Serf2*$^{+/+}$ and *Serf2*$^{+/-}$ from E15.5
136 until birth (Two-way ANOVA: E17.5 WT vs KO p_{bon}<0.05; P0 WT vs ko p_{Bon}<0.0001) (Figure 1E,
137 S1D-E). No differences in size could be observed between *Serf2*$^{+/+}$ and *Serf2*$^{+/-}$ embryos during the
138 embryonic stage leading up to birth (P0). Histological examination of various tissues revealed a
139 developmental delay of approximately one to two days in the organs of E17.5 *Serf2*$^{-/-}$ embryos
140 compared to the previous time points and standard embryonic development(Kaufman, 1992; Kaufman
141 & Bard, 1999). This was most prominently in the lungs, through reduced expansion of alveoli and

142 augmented tissue density, and in the kidneys, by the increased amount of mesenchyme between the
143 tubules and glomeruli (Figure S1F). At the time of birth, the lungs of *Serf2*$^{-/-}$ pups displayed a
144 significantly reduced saccular space (t-test: p= 0.0088) (Figure 1F), reflecting insufficient lung
145 expansion and maturation. This partial fetal atelectasis seems to explain the observed respiratory
146 distress and a likely cause of the perinatal lethality in *Serf2*$^{-/-}$ pups. Placental abnormalities have been
147 shown to cause impaired transfer of nutrients and oxygen to the embryo, resulting in growth
148 delays(Ward *et al*, 2012). To exclude this as a potential cause, we examined the placenta at all three
149 embryonic stages for microscopic lesions in the placental labyrinth or other changes. No genotype-
150 related pathology could be found, indicating that absence of SERF2 in the embryo itself is responsible
151 for the observed growth phenotype. This seems to be supported by the fact that CRISPR-induced
152 *Serf2*$^{-/-}$ clones of HEK293T cells display a delay in proliferation (Figure S2A). Moreover, RNA
153 sequencing analysis of mouse embryonic fibroblasts (MEF) isolated from E13.5 embryos showed a
154 clear enrichment of GO-terms clustered around three closely related biological functions: cell cycle,
155 cell proliferation and cell adhesion (Supplemental Figure S2A-B). Interestingly, in the cell cycle
156 cluster we observe an overall upregulation of factors driving cell division and downregulation of
157 growth arrest factors in *Serf2*$^{-/-}$ MEFs (Supplemental Table 2). This observation seems in line with a
158 developmental delay phenotype in *Serf2*$^{-/-}$ mice, because it is known that cell proliferation is favored
159 over differentiation in earlier stages of embryonic development compared to later stages(Ciemerych &
160 Sicinski, 2005). Overall, the cell culture results point towards a cell-autonomous effect of SERF2 and
161 suggest that loss of *Serf2* results in delayed growth. While our previous study also demonstrated a cell-
162 autonomous function for moag-4, it did not show any effects of moag-4 deletion on the viability, life
163 span or size of *C. elegans*(van Ham *et al*, 2010). All together, our results suggest that *Serf2* KO causes
164 delayed maturation of certain organs at the time of birth resulting in death. Given the cell-autonomous
165 nature of the effects of SERF2, we aimed to avoid these adverse effects by creating an organ-specific
166 conditional KO model.

167 *Brain-specific KO of Serf2 does not affect viability or the Aβ production pathway*

168 To study the effect of *Serf2* KO on amyloid pathology in the brain, we circumvented the perinatal
169 lethality of full-body *Serf2* KO mice by generating a brain-specific *Serf2* KO mouse model (*Serf2*$^{br-/-}$).
170 The conditional KO was obtained by combining our *Serf2*$^{flox/flox}$ mice with a *Sox1-Cre*
171 model(Takashima *et al*, 2007) (Figure S3A). SOX1 is one of the earliest transcription factors
172 expressed in neuronal precursors of the ectoderm from embryonic day 7.5(Pevny *et al*, 1998; Wood &
173 Episkopou, 1999). Consequently, the *Sox1* promotor was selected as a pan-neuronal driver of
174 Recombinase cre expression to restrict homologous recombination to the central nervous
175 system(Takashima *et al*, 2007). Analysis of *Serf2* expression on the mRNA and protein level in
176 various organs confirmed brain-specific ablation of *Serf2* by *Sox1*-mediated *Cre* expression in our
177 *Serf2*$^{flox/flox}$ mice (t-test WT vs *Serf2*$^{br-/-}$ brain: 1m p=0.0022; 3m p=0.00527) (Figure S3B-C). This
178 conditional KO was crossed with the *APPPS1-21* amyloid (AM) model(Radde *et al*, 2006), which
179 contains human transgenes for both APP with the Swedish KM670/671NL mutation and PSEN1 with
180 the L66P mutation. From this cross we obtained four experimental groups: WT, *Serf2*$^{br-/-}$, AM and
181 AM;*Serf2*$^{br-/-}$ (Figure 2A). Upon crossing of the *Serf2*$^{br-/-}$ with the amyloid model, we observed the
182 expected Mendelian ratio for all the genotypes at P22, indicating that the viability is not significantly
183 affected by brain-specific KO of *Serf2* (Chi Square: p= 0.37)(Supplemental Table 3). Based on the
184 known progression of Aβ plaque pathology in the AM mice, we selected two age groups for further
185 analysis: before (1 month) and after (3 months) Aβ plaque deposition (Figure 2B). Analysis of the
186 *Serf2* mRNA levels in both age groups showed that *Serf2* expression was not altered by the plaque
187 pathology and confirmed the KO in the *Serf2*$^{br-/-}$ and AM;*Serf2*$^{br-/-}$ mice. Some residual *Serf2*
188 expression could be detected in the brains of the KO groups likely due to the presence of cells from
189 non-neuronal lineage in the samples, e.g. cells from circulatory system (Two-way ANOVA: *Serf2*$^{br-/-}$
190 and AM;*Serf2*$^{br-/-}$ vs WT 1m p_{bon} <0.001; 3m p_{bon} <0.0001) (Figure 2C). These results were also
191 confirmed on the protein level using western blot (Figure 2D). In accordance with the effects observed
192 in the full-body *Serf2*$^{-/-}$ mice, the *Serf2*$^{br-/-}$ and the AM;*Serf2*$^{br-/-}$ mice did show a reduction in brain
193 weight compared to WT in both age groups (Two-way ANOVA: *Serf2*$^{br-/-}$ vs WT both ages p_{bon}<0.01;
194 AM;*Serf2*$^{br-/-}$ vs WT 1m p_{bon}<0.0001; 3m p_{bon}<0.001) (Figure 2E). While the weight reduction seems
195 to be slightly more pronounced in AM;*Serf2*$^{br-/-}$ compared to *Serf2*$^{br-/-}$, AM by itself displayed no

196 significant change in brain weight. This would indicate that *Serf2* ablation, *Cre* expression or a
197 combination of both is most likely responsible for the difference in weight. However, AM mice may
198 be more susceptible to this effect (Figure 2E). To distinguish between the effects of *Cre* expression
199 and *Serf2* KO, we also examined the *Sox1-Cre* mice(Takashima *et al*, 2007) without floxed *Serf2*
200 (*Cre*^{br}) and crossed them with *APPPS1-21*(Radde *et al*, 2006) without floxed *Serf2*. The *Cre*^{br} mice
201 also showed a reduction in brain weight compared to the WT controls, which was more pronounced at
202 1 month (One-Way ANOVA: *Cre*^{br} vs WT 1m $p_{bon}<0.05$) (Figure S3D), but was overall less extensive
203 than the reduction in *Serf2*$^{br-/-}$ animals (One-way ANOVA: *Cre*^{br} vs WT $p_{bon}<0.01$; AM;*Cre*^{br} vs WT
204 $p_{bon}<0.001$) (Figure 2F). Together, this suggests that *Cre* expression is partially responsible for the
205 observed decrease in brain size, particularly at 1 month of age. Due to ongoing brain maturation
206 between 1 and 3 months, all groups show a significant increase in brain weight (Two-way Anova: Age
207 $p<0.0001$), but this maturation appeared unaffected by *Serf2* KO. Moreover, the difference in brain
208 weight between WT and *Serf2*$^{br-/-}$remained constant beyond the age of 3 months up to 11 months of
209 age (Figure S3E). This suggests that the reduction in brain size takes place during specific stages of
210 brain development, but that the continued development is not necessarily altered by these changes.
211 Additional histological examination of the brains with hematoxylin-eosin staining revealed no
212 difference in the cell density (Figure 2G), nor did we find any evidence of degeneration, apoptosis or
213 necrosis. Apart from the overall reduction in weight, the brains showed no structural abnormalities and
214 the tissue appeared healthy.

215 Next, we examined whether the brain KO of *Serf2* affected any of the key components in the Aβ
216 aggregation process, like altering the levels of APP or the production of its cleavage products, $A\beta_{40}$
217 and $A\beta_{42}$. We determined the expression of human *APP* in WT, *Serf2*$^{br-/-}$, AM and AM;*Serf2*$^{br-/-}$ mice
218 at both 1 and 3 months of age and observed no difference due to brain specific *Serf2* KO (t-test: 1m
219 p=0.9170; 3m p=0.9963) (Figure 2H, data from WT, *Serf2*$^{br-/-}$ not included due to lack of APP
220 construct and absence of signal). Western blot analysis confirmed there was also no difference in APP
221 protein levels between AM and AM;*Serf2*$^{br-/-}$ (t-test: 1m p= 0.1157;3m p=0.5908) (Figure 2I and J).
222 Further analysis of $A\beta_{40}$ (Two-way ANOVA: Genotype p=0.8841; Age $p<0.0001$;Interaction

223 p=0.8841) (Figure 2K) and $A\beta_{42}$ (Two-way ANOVA: Genotype p=0.7006; Age p<0.0001 ;Interaction
224 p=0.6522) (Figure 2L) showed an increase in concentration between 1 and 3 months, but this was the
225 same in both AM and AM;*Serf2*$^{br-/-}$. Given the variability in the Aβ concentrations at 3 months and the
226 fact that the ratio between these two peptides is known to affect the aggregation process, we also
227 investigated the correlation between these two Aβ levels (Figure 2M). This analysis showed that mice
228 with a high $A\beta_{42}$ concentration display a similarly high $A\beta_{40}$ level, maintaining a comparable $A\beta_{40}$
229 /$A\beta_{42}$ ratio for both AM and AM;*Serf2*$^{br-/-}$ animals. Taken together, this data suggests that SERF2 does
230 not affect the levels of APP and its cleavage products, $A\beta_{40}$ and $A\beta_{42}$. These findings are in accordance
231 with the previously observed effects of MOAG-4 on the aggregation of polyglutamine, Aβ and αSyn
232 in *C. elegans*, which modifies the aggregation process without changing the overall levels of these
233 aggregation-prone proteins(van Ham *et al*, 2010). While the difference in brain size is definitely a
234 factor to be considered during further analysis, given the fact that we observed no obvious changes in
235 the overall health, continued development and APP processing pathway of these brain-specific *Serf2*
236 KO mice, we proceeded with our analysis of Aβ pathology in these animals.

237 *Serf2 KO alters the amount of Aβ deposition in the brain*

238 We next investigated whether SERF2 affects the Aβ aggregation by performing immunohistological
239 analysis of the Aβ plaque pathology. Initially, we performed a general Aβ staining using the 6E10
240 antibody. In accordance with the known progression of Aβ plaque pathology in the amyloid model, we
241 only found extracellular deposits in the 3-month-old AM and AM;*Serf2*$^{br-/-}$ mice. As expected, most
242 plaques were found in the cortex, with some pathology beginning to spread to the hippocampus as
243 well (Figure S4). Microscopic inspection of the Aβ deposits revealed a broad range of sizes with a
244 wide variety in staining intensity and patterns, but we found no clear morphological differences
245 between the plaque population found in AM and AM;*Serf2*$^{br-/-}$ (Figure 3A, S4). Quantification of the
246 6E10-positive deposits showed a slight increase in AM;*Serf2*$^{br-/-}$ compared to AM, but this just failed
247 to reach statistical significance in the Bonferroni corrected post-hoc comparison (Two-way ANOVA:
248 all 3m non-AM vs AM groups p_{bon} <0.0001; AM vs AM;*Serf2*$^{br-/-}$ p_{bon} =0.063)(Figure 3B). Given the
249 high variability in plaque load between animals within the same experimental group, we examined

250 whether this variability reflected the previously observed variation in Aβ levels. Unsurprisingly,
251 animals with higher levels of $A\beta_{40}$ (Figure 3C) and $A\beta_{42}$ (Figure 3D) displayed a higher overall plaque
252 load in both groups. More interestingly, our linear regression analysis revealed that AM;*Serf2*$^{br-/-}$ mice
253 tend to have a significantly higher plaque load than AM mice with similar Aβ levels (Supplemental
254 Table 4). A second general Aβ stain with the W0-2 antibody displayed a similar slight increase in the
255 amount of plaque deposits in AM;*Serf2*$^{br-/-}$ at 3 months (Two-way ANOVA: all 3m non-AM vs AM
256 groups p_{bon} <0.0001; AM vs AM;*Serf2*$^{br-/-}$ p_{bon} =0.101) (Figure 3E). In fact, a comparison between the
257 6E10 and the W0-2 staining in individual animals confirmed the similarity between both staining
258 patterns at 3 months (Figure 3F, S5, Supplemental Table S3). Interestingly, our detection algorithm
259 also picked up a small increase in the counts of W0-2-positive foci in the 1 month AM;*Serf2*$^{br-/-}$ group
260 (Two-way ANOVA: 1m WT vs AM;*Serf2*$^{br-/-}$ p_{bon} =0.088 ; *Serf2*$^{br-/-}$ vs AM;*Serf2*$^{br-/-}$ p_{bon} =0.081; AM
261 vs AM;*Serf2*$^{br-/-}$ p_{bon} =0.127; all other comparisons p_{bon} >0.999) (Figure 3E). Closer examination of the
262 microscopic images revealed the identified spots were not extracellular plaques, but were the result of
263 increased levels of W0-2-positive intracellular staining in AM;*Serf2*$^{br-/-}$ (Figure S7A). Some low level
264 intracellular W0-2 and 6E10 staining could also be observed in the other 1-month-old AM mice, but
265 not to the extent that it was picked up by the detection algorithm (Figure S7A-B). This would suggest
266 that the deletion of *Serf2* already alters the intracellular accumulation of Aβ prior to plaque deposition.
267 Overall, these results indicate that the presence of SERF2 is indeed able to modify Aβ aggregation in
268 the mouse brain.

269 *SERF2 deficiency changes the proportion of ThS-positive cores, but not the immunoreactivity*
270 *of deposits*

271 To investigate if SERF2 also affected the amount of Thioflavin-positive fibrils, we performed
272 Thioflavin-S (ThS) staining. Here, we again observed a large variety in the amount of ThS-positive
273 plaques between individual animals, but we found no mean difference between AM and AM;*Serf2*$^{br-/-}$
274 mice (Two-way ANOVA: all 3m non-AM vs AM groups p_{bon} <0.001) (Figure 3G). However, further
275 analysis of the correlation between Aβ levels and the amount of ThS-positive plaques revealed that
276 AM mice showed a positive correlation similar to the general Aβ stainings, while AM;*Serf2*$^{br-/-}$ mice

277 displayed an inverse relationship (Figure 3H, 3I, Supplemental Table S3). Consequently, a general
278 increase in Aβ deposits does not equate to an increase in amyloid deposition in AM;*Serf2*$^{br-/-}$ mice, as
279 it does in AM mice (Figure 3J), further demonstrating a change in the amyloid formation in *Serf2* KO
280 mice. In addition, we investigated microglia activation and whether we could detect a change in the
281 gliosis associated with Aβ plaques. Staining for Iba1 showed a slight increase in the AM;*Serf2*$^{br-/-}$ mice
282 compared to AM (Two-way ANOVA: 3m non-AM groups vs AM p_{bon} <0.01; non-AM groups vs
283 AM;*Serf2*$^{br-/-}$ p_{bon} <0.0001; AM vs AM;*Serf2*$^{br-/-}$ p_{bon} <0.01) (Figure 3K), similar to what was observed
284 with the 6E10 staining (Figure 3B). We therefore examined if this increase was simply related to the
285 increase in Aβ deposits or if AM;*Serf2*$^{br-/-}$ also displayed a different immune response to plaques
286 compared to AM. Our analysis revealed a similar correlation between 6E10-positive deposits and
287 immune response for AM and AM;*Serf2*$^{br-/-}$ mice, suggesting the deposits evoked a similar immune
288 response in both groups(Figure S6A, Supplemental Table S3).

289 *Knockout of Serf2 changes the plaque composition and fibril structure*

290 Given the differences in the reactivity of the Aβ deposits between the various stains, we decided to
291 explore the composition within the individual plaques in greater detail. To this end, we made use of
292 two luminescent conjugated oligothiophenes (LCO), qFTAA (quadro-formylthiophene acetic acid)
293 and hFTAA (hepta-formylthiophene acetic acid). These LCOs are small hydrophobic ligands with a
294 high affinity for binding distinct types of amyloids and can easily be distinguished from each other
295 based on their spectral properties(Klingstedt *et al*, 2011). The smallest of the two molecules, qFTAA,
296 is characterized by a peak in its emission spectrum around 500 nm and has been shown to stain
297 compact, multifilament fibril structures, coinciding with ThT and Congo red staining(Psonka-
298 Antonczyk *et al*, 2016; Nyström *et al*, 2013; Klingstedt *et al*, 2011). Whereas hFTAA emits in the
299 yellow to red range with a peak around 600 nm and is capable of staining prefibrillar (non-
300 thioflavinophilic) and single fibril aggregates found during the lag-phase of in vitro ThT kinetics
301 (Figure 4A). The prefibrillar aggregates were shown to be stained with 6E10, but not Congo red, ThT
302 or qFTAA(Klingstedt *et al*, 2011; Nyström *et al*, 2013; Psonka-Antonczyk *et al*, 2016). Previous
303 studies have shown that by combining LCO dyes it is possible to uncover structural differences in

304 plaque composition(Lord *et al*, 2011; Nyström *et al*, 2013; Rasmussen *et al*, 2017). We performed
305 confocal spectral imaging of randomly selected plaques in 3-month-old AM and AM;*Serf2*$^{br-/-}$ mice
306 after double staining with both LCOs and determined the ratio of the light intensity emitted at 502nm
307 and 588nm as a measure for the relative amounts of fibrillar and prefibrillar aggregates within the
308 individual plaques. An exploratory frequency analysis of the intensity ratios found in both groups
309 revealed a three-peak pattern in which the middle peak was similarly represented in both groups
310 (Figure 4B, green area). The first peak, however, was predominantly found in AM mice (Figure 4B,
311 red area), while the third peak was mainly detected in AM;*Serf2*$^{br-/-}$ (Figure 4B, blue area). This shift
312 in ratio was also reflected by a significant difference in the average intensity ratio between AM and
313 AM;*Serf2*$^{br-/-}$ (t-test $p<0.001$) (Figure 4C). This increase in intensity ratio could not be observed in
314 AM;*Cre*^{br} mice (t-test $p=0.6047$) (Figure 4C, insert), indicating that this effect is caused by the *Serf2*
315 KO and unrelated to *Cre* expression. Given the fact that AM;*Cre*^{br} animals also show a decrease in
316 brain weight without a change in LCO staining, this would also suggest that the weight reduction is
317 not a factor in these results. Although, as the change in brain weight is more pronounced in *Serf2*$^{br-/-}$
318 animals, we cannot completely exclude this as a potential contributing factor. Next, we examined if
319 the change in the intensity ratio correlated with the slight increase in 6E10-positive deposits we
320 observed in AM;*Serf2*$^{br-/-}$ (Figure 4D). However, the higher average intensity ratio in AM;*Serf2*$^{br-/-}$
321 mice was not related to this general plaque load nor the number of W0-2- or ThS-positive deposits
322 (Figure S6B, S6C). Further microscopic analysis of low intensity ratio deposits from AM mice showed
323 a plaque with a qFTAA- and hFTAA-positive core and a border that was only stained by hFTAA
324 (Figure 4E, left panels). The high intensity ratio deposits from AM;*Serf2*$^{br-/-}$ mice, on the other hand,
325 revealed a qFTAA-positive core, but virtually no hFTAA-staining (Figure 4E, right panels),
326 demonstrating the difference in plaque composition reflected by the shift in LCO intensity ratios.
327 Additionally, we visualized the global fibrillar structure of the plaques on a nanometer scale using
328 high resolution, scanning transmission electron microscopy (STEM). Overall, STEM images of
329 plaques from AM;*Serf2*$^{br-/-}$ tended to show more condensed plaques composed of short, thick and
330 densely packed bundles of fibers with little space in between (Figure 4F, right panels). In the AM
331 mice, however, the plaques we observed displayed more loosely packed fibrils (Figure 4F, left panels).

332 Taken together, these findings suggest *Serf2* KO in mice leads to a shift in the Aβ aggregation process,
333 resulting in an altered structural composition of the plaques.

334 **Discussion**

335 Previous studies identified MOAG-4 and its human orthologs SERF1A and SERF2 and their potential
336 to modify the aggregation of amyloidogenic proteins. While the exact endogenous biological function
337 of these peptides remains unclear, a recent study has provided evidence for RNA-binding properties of
338 SERF1A through a region which is highly conserved in MOAG-4 and SERF2(Meyer *et al*, 2019). In
339 this study, we have demonstrated in cells and mice that SERF2 provides a growth advantage during
340 development. The absence of SERF2 or MOAG-4 in itself does not appear to be lethal in cells, worms
341 or the brain-specific KO mice. Therefore, we postulate that the observed perinatal lethality in the full-
342 body KO mice is a secondary effect of the delay in growth due to insufficient maturation of certain
343 organs at birth. This appears to be supported by the fact that some pups survived the initial minutes
344 after birth and incomplete penetrance of the lethality in the earliest generations with mixed genetic
345 background. The 129SV genetic background present in these mice is known to have a gestation period
346 that is on average around one day longer than C57/Bl6J mice(Murray *et al*, 2010), which could result
347 in improved lung maturation. While the exact function of SERF2 remains unknown, we propose its
348 effects on growth and development are most likely caused through one of two mechanisms: either
349 SERF2 facilitates cell proliferation or it protects cells from stressors that create an unfavorable
350 environment for cell division. In the latter case, we would expect to see an upregulation of stress
351 pathways or cell cycle arrest proteins inhibiting the cell cycle in *Serf2*$^{-/-}$ cells. Interestingly, the RNA
352 seq analysis of the MEFs from our *Serf2*$^{-/-}$ mice showed the exact opposite. Cell cycle driving factors
353 were upregulated (e.g. cyclins). Whereas, stress signaling and cell cycle inhibiting factors were
354 downregulated (e.g. GADD45 and GAS1). Thus, the *Serf2*$^{-/-}$ cells actually displayed an increased
355 stimulation of cell proliferation mechanisms, which would fit with cells from earlier stages of
356 embryonic development. This would suggest the first mechanism, with a beneficial role for SERF2 in
357 the efficient execution of cell proliferation, as the most likely explanation for the observed growth
358 effect. Furthermore, an increase in cellular stress would most likely result in decreased health and

359 fitness. However, *moag-4* deletion worms showed no changes in life span compared to controls(van
360 Ham *et al*, 2010) and, apart from the initial growth deficit, the tissues of *Serf2* KO mice appeared
361 healthy and continued to develop similarly to controls after birth. A recent study showed SERF1a
362 might play a role as an RNA-organizing protein, which localizes to membraneless nuclear organelles,
363 like the nucleolus, under normal physiological conditions. However, under stress conditions, it was
364 shown to migrate to the cytoplasm, where it could drive amyloid toxicity.(Meyer *et al*, 2019) While
365 there was no compensatory upregulation of SERF1 in response to SERF2 KO and a similar mode of
366 action remains to be demonstrated for SERF2, the structural homology of the two proteins would
367 suggest a comparable function. Given the importance of nucleolar disassembly and reassembly in cell
368 cycle control(Visintin & Amon, 2000; Leung *et al*, 2004), an RNA-organizing function could explain
369 how SERF2 facilitates cell proliferation. This developmental role would have limited biological
370 importance in non-proliferating, differentiated cells, like the brain's neurons or the cells of adult *C.*
371 *elegans*, and might also explain why we saw no adverse effects in the *moag-4* deletion worms or our
372 adult *Serf2*$^{br-/-}$ mice. While a reduced biological importance of SERF2 later in life could prove
373 interesting with regard to the treatment of age-related neurodegenerative disorders, further exploration
374 of SERF2's endogenous function and how it evolves with ageing will be needed to fully assess this
375 mechanism's therapeutic potential.

376 In this study, we confirmed the ability of SERF2 to modify the Aβ pathology *in vivo* in a mouse model
377 without changing the overall Aβ levels. We showed that mice lacking SERF2 were more prone to
378 form Aβ deposits and that the composition of these deposits was structurally different. In AM mice
379 higher levels of Aβ result in an increase in the numbers of Aβ deposits as well as an increase in the
380 number of ThS-positive deposits. AM;*Serf2*$^{br-/-}$ mice, on the other hand, also show an increase in Aβ
381 deposits, but this did not lead to higher numbers of ThS-positive plaques, indicating an altered
382 dynamic for amyloid formation. These findings were further corroborated by the LCO spectra, which
383 revealed that the plaques in AM;*Serf2*$^{br-/-}$ mice have a different conformation of pre-fibrillar and
384 fibrillar Aβ compared to AM mice. Finally, STEM imaging also confirmed a globally altered structure
385 of the amyloid fibrils in the plaques. Amyloid fibrils are formed through a nucleated self-assembly

386 process characterized by a structural conformation to a β-strand secondary structure and the formation
387 of a critical nucleus during the initial oligomerization. The nuclei act as seeds from which the fibrils
388 grow and have been shown to propagate a specific fibril structure(Petkova *et al*, 2005; Qiang *et al*,
389 2017). In vitro kinetic assays with SERF and MOAG-4 have shown that these peptides accelerate
390 aggregation by acting on the nucleation phase(Meinen *et al*, 2019; Falsone *et al*, 2012; Yoshimura *et*
391 *al*, 2017; Merle *et al*, 2019). Recently, we have shown that SERF2 is equally capable to drive amyloid
392 formation of α-Syn and Aβ *in vitro* through a conserved, positively charged region(Pras *et al*,
393 2020). Meanwhile, another study has demonstrated that binding of the intrinsically disordered protein
394 yeast SERF to α-Syn and Aβ results in fuzzy complexes with heterogeneous structural
395 conformations that are more extended in nature(Meinen *et al*, 2019). For α-Syn, the disruption of
396 intra-molecular electrostatic interactions by the positively charged region of MOAG-4/SERF1 was
397 found to expose an amyloid nucleation site(Merle *et al*, 2019; Yoshimura *et al*, 2017). Intra-molecular
398 electrostatic interactions have also been proven to play a part in the dynamics and structure of the Aβ
399 monomer folding, which is at the basis of nucleus formation. In fact, several of the familial AD
400 mutations located within the Aβ sequence and reported not to affect the Aβ levels, appear to exert their
401 effects by modifying the intra-molecular interactions and monomer folding(Grant *et al*, 2007; Lazo *et*
402 *al*, 2009; Elkins *et al*, 2016; Ni *et al*, 2011). These single amino acid modifications in the Aβ
403 sequences also result in alterations in the aggregation kinetics, fibril structure and aggregate toxicity in
404 *in vitro* studies(Ovchinnikova *et al*, 2011; Van Nostrand *et al*, 2001; Miravalle *et al*, 2000). Moreover,
405 patients and mouse models with these mutations show differences in the localization of Aβ
406 accumulation and deposition, as well as differences in its structure, giving rise to specific disease
407 phenotypes. For instance, while some mutations result in increased Aβ deposition and altered plaque
408 structure, other mutations at the same location result in cerebral amyloid angiopathy with Aβ
409 deposition in blood vessels rather than the brain parenchyma or even an absence of extracellular Aβ
410 deposition(Inayathullah & Teplow, 2011; Bugiani *et al*, 2010; Grabowski *et al*, 2001; Philipson *et al*,
411 2009; Shimada *et al*, 2011; Tomiyama *et al*, 2010; Grant *et al*, 2007; Ni *et al*, 2011; Nilsberth *et al*,
412 2001; Lord *et al*, 2011; Tomiyama *et al*, 2008; Van Nostrand *et al*, 2001). In addition, some of these

413 mutants showed increased intracellular Aβ accumulation which differed in structure-specific staining
414 characteristics(Lord *et al*, 2006; Kulic *et al*, 2012; Tomiyama *et al*, 2010). The differences in Aβ
415 pathology between these mutants seem to display some similarities to the changes we observed
416 between our AM and AM;*Serf2*$^{br-/-}$ mice. Together with the *in vitro* findings about the mechanism of
417 SERF2 interaction with aggregation-prone proteins, this would appear to suggest modulation of intra-
418 molecular interactions and altered nucleation as the mechanism for SERF2's effect on aggregation and
419 amyloid formation in our mice. Interestingly, there is increasing evidence that qualitative, structural
420 properties may be more related to toxicity than the quantity of aggregates and deposits. Recent studies
421 have provided increasing evidence that structural polymorphs are associated with differences in
422 toxicity and different clinical phenotypes in sporadic and familial cases(Lu *et al*, 2013; Cohen *et al*,
423 2015; Rasmussen *et al*, 2017; Qiang *et al*, 2017; Cohen *et al*, 2009). One recent study demonstrated
424 that these structural conformations of distinct disease phenotypes could also be detected by differences
425 in the LCO spectra of the plaques and that these spectral properties could, at least partially, be
426 transmitted to a mouse model through seeding(Rasmussen *et al*, 2017). While the effect of familial
427 mutations on the formation of distinct polymorphs has already been explored by others(Philipson *et al*,
428 2012; Lord *et al*, 2006; Kulic *et al*, 2012; Rasmussen *et al*, 2017), our study provides the first evidence
429 of a single endogenous factor, separate from Aβ and its production pathway, contributing to a
430 structural shift of amyloid pathology in a mammalian system. Further research will be needed to
431 elucidate the exact structural changes at an atomic level and if they affect toxicity and disease
432 progression similarly to what was previously observed in *C. elegans*. This will provide new insights
433 into the structural properties and diversity of disease-protein aggregation, contributing to a better
434 understanding of the variability in disease manifestation and open up previously unexplored avenues
435 for therapeutic research.

436 **Materials and methods**

437 *Animals*

438 *Serf2* knockout mice were generated by introducing *loxP* sites in the *Serf2* gene on either side of exon
439 2, in accordance with the 'knockout-first' allele design as described by Skarnes and
440 colleagues(Skarnes *et al*, 2011). Full-body *Serf2* knockout mice were obtained by crossing these
441 floxed mice with 129SV mice expressing *Cre* under the *Hprt* promoter, resulting in the removal of
442 exon 2 by *Cre*-mediated recombination (Figure S1A). Subsequently, these mice with mixed
443 background were backcrossed at least 6 times to a C57Bl/6J background. Homozygous and
444 heterozygous full-body *Serf2* knockout mice were examined with their wild-type littermates at
445 embryonic day 13.5, 15.5 and 17.5, as well as at the day of birth (P0) and day of weaning (P22).

446 Heterozygous *Sox1-Cre* mice(Takashima *et al*, 2007) were backcrossed at least 8 times to a C57BL/6J
447 background. These animals were also used as controls to differentiate between effects of *Cre*
448 expression and Serf2 knockout. To generate the conditional *Serf2* knockout mice, the floxed mice
449 were first crossed with Tg(ACTFLPe)9205Dym (Jackson#003800) mice to flip the FRT site and
450 remove the lacZ and neo cassette. Subsequently, these mice were backcrossed at least 6 times to a
451 C57BL/6J background. Finally, the resulting homozygous *Serf2*$^{flox/flox}$ mice were crossed with the
452 backcrossed *Sox1-Cre* mice, to obtain the brain-specific *Serf2* knockout mice (Figure S3A). The
453 conditional *Serf2* knockout mice were crossed with the APPPS1-21 transgenic mice (APP
454 (KM670/671NL)/PS1(L166P), Rottenburg, Germany) (Radde *et al*, 2006). A final cross between
455 heterozygous APPPS1-21; *Serf2*$^{flox/flox}$ and heterozygous *Sox1-Cre*; *Serf2*$^{flox/flox}$ resulted in four
456 experimental groups of *Serf2*$^{flox/flox}$ mice: *Sox1-Cre*$^{-/-}$; APPPS1-21$^{-/-}$ (WT), *Sox1-Cre*$^{+/-}$; APPPS1-21$^{-/-}$
457 (*Serf2*$^{br-/-}$), *Sox1-Cre*$^{-/-}$; APPPS1-21$^{+/-}$ (AM) and *Sox1-Cre*$^{+/-}$; APPPS1-21$^{+/-}$ (AM;*Serf2*$^{br-/-)}$ (Figure 2A).
458 All experimental groups were tested at 1 month or 3 months of age.

459 All experiments were approved by the Institutional Animal Care and Use Committee of the University
460 of Groningen (Groningen, The Netherlands). All mice were maintained on a C57BL/6J background
461 and housed in a 12:12 hour light/dark cycle and the animals had ad libitum access to food and water.
462 Genotyping of embryos was performed using tail and yolk sac biopsies. Otherwise, ear biopsies were
463 used. DNA was purified using prepGEM® Tissue kit according to a protocol adapted from the

464 manufacturer (ZYGEPTI0500, ZyGEM, VWR International BV) and subjected to PCR using the
465 primers listed in Supplemental Table S5. Mice were terminated through CO_2-inhalation and cervical
466 dislocation for subsequent tissue collection.

467 *Embryo processing and histochemistry*

468 Embryos were fixed in 4 % formalin (Kinipath) for a minimum of 24 hours at room temperature. For
469 the pathological analysis, the embryos and their placenta were bisected longitudinally and embedded
470 in paraffin. Using the microm HM 340E (Thermo Scientific) 4 µm sections were cut for the
471 hematoxylin-eosin (HE) staining. The HE sections were incubated at 60 °C for 15 minutes. Next,
472 sections were deparaffinized and rehydrated in xylene (2x), 100 % alcohol (2x), 96 % alcohol, 70 %
473 alcohol and water. HE staining was performed by incubation with hematoxylin for 4 minutes, water
474 for 10 minutes, eosin for 1 minute and water for 10 seconds. After staining all sections were
475 dehydrated in 70 % alcohol, 96 % alcohol, 100 % alcohol (2x) and xylene (2x).

476 *Brain processing*

477 Upon termination, all brains were collected and weighed. From each experimental group three whole
478 brains were collected for HE staining according to the protocol described under embryo processing.
479 HE-stained sections were scanned with the TissueFAXs microscope using 20X objective. Images were
480 processed for nuclei counts using Histoquest software. The remaining brains were divided sagittally.
481 The left hemibrain was prepared for histochemistry and fixed in 4 % paraformaldehyde (PFA) for 48
482 hours at room temperature on a shaker. Next, the brains were placed in 30 % sucrose for
483 approximately 12 hours. Afterwards, the excess sucrose was removed and hemibrains were frozen in
484 molds with Tissue Tek O.C.T. compound (Sakura, The Netherlands) on dry ice. The right hemibrain
485 was snap frozen in liquid nitrogen and stored at -80°C. This tissue was homogenized using a liquid
486 nitrogen cooled mortar for subsequent protein and RNA analysis.

487 *Quantitative RT-PCR*

488 Total RNA was extracted from snap frozen tissue using TRIzol Reagent (Life Technologies) according
489 to the manufacturers' description. Total RNA quality and concentration were assessed using a
490 NanoDrop 2000 spectrophotometer (Thermo Scientific/Isogen Life Science). cDNA was made from
491 1,5 µg total RNA with a RevertAid H Minus First Strand cDNA Synthesis kit (Thermo Scientific)
492 using random hexamer primers. Quantitative real-time PCR was performed using a Roche LightCycler
493 480 Instrument II (Roche Diagnostics) with SYBR green dye (Bio-Rad Laboratories) to detect DNA
494 amplification. Relative transcript levels were quantitated using a standard curve of pooled cDNA
495 solutions. Expression levels were normalized to β-Actin or 18S mRNA levels. The primers for
496 Quantitative PCR used are listed in Supplemental Table S5.

497 *Western Blot analysis*

498 For SERF2 analysis tissues were homogenized in RIPA buffer (50 mM Tris pH 8, 150 mM NaCl,
499 5mM EDTA, 0.5 % SDS, 0.5 % SDO, 1 % NP-40) with protease inhibitor cocktail (Roche) and
500 incubated on ice for 1 hour, spun down at 13,300 rpm for 30 minutes at 4 °C and the supernatant was
501 collected. Protein measurements were performed using a BCA kit (Pierce) and 150 µg was loaded on a
502 10-20 % tris/tricine SDS-page gels (Bio-Rad Laboratories) and blotted onto 0,2 µm nitrocellulose
503 membrane (Bio-Rad Laboratories). Membranes were incubated overnight with SERF2 (1/1500,
504 Protein tech) or Actin (1/10 000, MP biomedicals) antibody. Next, the membranes were incubated
505 with anti-mouse or –rabbit secondary antibodies tagged with horseradish peroxidase (1/10 000, Bio-
506 Rad Laboratories) for one hour at room temperature and visualized by chemiluminescence (Amersham
507 ECL prime western blotting detection reagent, VWR).

508 *RNA sequencing*

509 RNA sequencing analysis was performed on three MEF cell lines from *Serf2*$^{-/-}$ mice and four *Serf2*$^{+/+}$
510 littermate controls. Total RNA was isolated from MEFs using the Qiagen RNeasy isolation kit.
511 Integrity of the RNA based on RIN scores as determined by a Bioanalyzer (Agilent). RNA-sequencing
512 libraries were prepared using TruSeq Stranded Total RNA with Ribo-Zero Human/Mouse/Rat (RS-
513 122-2201; Illumina, CA, USA) according to manufacturers' protocol. Pooled libraries were sequenced

514 on an Illumina HiSeq 2500 (single-end 50 bp). Reads were aligned to the mouse reference genome
515 (mm10) using a splicing-aware aligner (StarAligner). Aligned reads were normalized to fragments per
516 million (FPM), excluding low abundance genes (mean FPM>1 in at least two samples). The raw count
517 data were pre-processed using the programming language R (3.4.0) [R Core Team, 2016, available
518 online at: www.r-project.org], the program RStudio (1.0.143) [RStudio Team, 2016, available online
519 at: http://www.rstudio.com/] and the EdgeR package (3.18.0)(Robinson et al., 2010). Genes that
520 displayed FPM value >1 in at least two libraries were retained, resulting in a list of 12,808 genes for
521 differential analysis. Differentially expressed (DE) genes between the *Serf2*$^{+/+}$ and *Serf2*$^{-/-}$ MEFs were
522 identified using the EdgeR general linear model approach. After statistical correction for multiple
523 comparisons with the "false discovery rate" (FDR) method (FDR<0.05), a list of 738 DE genes was
524 obtained. DAVID (6.8) was used to perform functional annotation analyses on this gene list and to
525 identify significantly enriched gene ontology (GO) terms [using GOTERM_BP_DIRECT] (Huang *et*
526 *al*, 2009b, 2009a). The connectivity between the enriched GO terms was further examined by
527 determining the amount of associated genes found (AGF) that were shared between two GO terms.
528 The most significant relationships (where a GO term shared > 25 % of the AGF) were mapped in a
529 network using the igraph package (1.0.1). The color of the edges reflects the major node, with the
530 largest amount of AGF, in each relationship. The weight of the edges was determined by the
531 percentage of AGF shared by the minor node in the relationship. We defined three clusters of GO-
532 terms, where multiple minor GO-terms connected to one or two central, major GO-terms . Minor GO-
533 terms were always clustered with the major GO-term with whom they shared the strongest connection.
534 One GO term, positive regulation of the apoptotic process, showed no direct relation with one of the
535 major GO-terms and was therefore assigned to the only cluster it had a significant connection with
536 (Figure S2A-B). RNA-seq data have been deposited in the ArrayExpress database at EMBL-EBI
537 (www.ebi.ac.uk/arrayexpress) under accession number E-MTAB-10083.
538 (http://www.ebi.ac.uk/arrayexpress/experiments/E-MTAB-10083)

539 ***[to be deleted] Upon acceptance of this work the data will be open access available, without***
540 ***password. Pending acceptance, the website can only be accessed by collaborators and reviewers***

541 *ELISA*

542 The ELISA experiments were performed as described previously(Huang *et al*, 2015). Briefly, the
543 frozen brain samples were homogenized in tissue protein extraction reagent (Pierce) supplemented
544 with complete protease inhibitors (Roche), and centrifuged for 1 hour at 430 000 g at 4 °C. The
545 supernatant was used for ELISA. The $A\beta_{40}$ and $A\beta_{42}$ levels were determined by standard sandwich
546 ELISAs using end-specific antibodies (Janssen Pharmaceutical), and the monoclonal JRFcAβ_{40}/28 and
547 JRFcAβ_{42}/26 antibodies as the capture antibodies. Horseradish peroxidase conjugated JRFAβN/25 or
548 JRFAβN/25 were used as the detection antibodies for, respectively, human Aβ or murine Aβ. Samples
549 were loaded in triplicate for each ELISA. The ELISAs were performed in triplicate for the 3-month-
550 old animals and in duplicate for the 1-month-old animals.

551 *Brain immunohistochemistry*

552 To evaluate Aβ-related pathology, the brain was cut in 30 µm thick serial cryostat sections. A series of
553 sections was selected with 300 µm spacing between individual sections and blind-coded, 6 per mouse
554 for the 6E10 and Iba1 antibody and 3 per mouse for W02. Sections were fixed in 4 % PFA for 10
555 minutes, followed by 20 minutes antigen retrieval in citrate acid (pH 6.0) and 30 minutes in 1 % H_2O_2
556 in methanol. Next the sections were incubated for 1 hour in 10 % goat or donkey serum, depending on
557 the secondary antibody, and immunolabeled overnight with antibodies against Aβ, and Iba1
558 (Supplemental Table S6). The sections were washed and incubated with the complementary
559 biotinylated secondary antibody (1/500, Jackson Immunoresearch) for 2 hours. Next, sections were
560 incubated in ABC complex and reacted with diamino-benzidine (0.5 mg/ml H2O with 0.01 % H_2O_2).
561 The stained sections were scanned with the TissueFAXs microscope using 20X objective. All images
562 were analyzed using the Fiji platform of the ImageJ software(Schindelin *et al*, 2012). For unbiased
563 feature detection we used a single automated script with optimized threshold method and parameters
564 for the complete image set of each staining method.

565 *Thioflavin-S Staining*

566 A 300 μm-spaced series of three blind-coded 30 μm sections were fixed in 4 % PFA for 10 min,
567 followed by incubation in 0.25 % potassium permanganate solution for 15 min, and a bleaching step
568 with 1 % potassium metabisulfite/1 % oxalic acid for 5 min, incubation with 0.02 % Thioflavin-S
569 solution in 50 % ethanol (Sigma T1892) for 8 minutes, rinsed with water between every step. Finally
570 the sections were incubated with 1 μl/ml DAPI. The sections were analyzed as described for the
571 immunostained sections. Stained sections were scanned with the TissueFAXs microscope using 20X
572 objective. Images were processed using Tissuequest software, selecting the cortex for automated
573 analyses.

574 *Luminescent conjugated oligothiophene (LCO) staining*

575 For the Luminescent conjugated oligothiophenes (LCO) stainings, two different LCO variants,
576 qFTAA (quadro-formyl thiophene acetic acid) and hFTAA (hepta-formyl thiophene acetic acid) were
577 used. Blind-coded 30 μm sections were double-stained with qFTAA and hFTAA (2.4 μM qFTAA and
578 0.77 μM hFTAA in PBS) similar to a previous description (Nyström et al., 2013). Sections were
579 incubated for 30 minutes in the dark at room temperature. Stainings were analyzed on the Zeiss LSM
580 510 META confocal microscope equipped with an argon 458 nm laser (Carl Zeiss MicroImaging
581 GmbH, Jena, Germany). An 40x objective (oil-immersion, 1.3 NA, Zeiss) was used for spectral
582 imaging of the Aβ deposits. Stacked images were acquired every 10 nm in the emission spectrum
583 between 470 to 695 nm. Locations were selected randomly from the plaque containing regions of the
584 temporal, frontal and occipital cortex. Images were analyzed using Fiji (Schindelin et al., 2012, 2015)
585 and standard computer algorithms to provide a reproducible, unbiased detection of the plaques. First,
586 the stacks of images across the different wavelengths of the spectrum were combined into one image
587 using the Z-projection sum. A threshold was applied to the resulting image using the "Triangle dark"
588 algorithm to automatically identify and delineate the plaques. Partial plaques on the edge of the images
589 and particles smaller than 25 μm^2 were excluded. These settings allowed us to detect over 98 % of all
590 the plaques in the images. The missed plaques were either too small or too low in intensity to be
591 accurately distinguished from the background. Incorrectly identified particles due to (lipofuscin) auto
592 fluorescence were readily identified based on their wavelength intensity profile and visual inspection

593 and were also excluded from the analysis. We identified between 17-25 plaques in each animal for the
594 spectral intensity measurements. The ratio of the intensity of emitted light at the blue-shifted portion
595 (502 nm) and red-shifted peak (588 nm) was used as a parameter for spectral distinction of different
596 Aβ deposits. These peaks of the spectra were selected to maximize the spectral distinction.

597 *Large-scale STEM (nanotomy)*

598 The scanning transmission electron microscopy (STEM) experiments were adapted from previously
599 described experiments (Kuipers et al., 2015). Briefly, paraffin embedded cortical sections of AM and
600 AM;*Serf2*$^{br-/-}$ were deparaffinized and postfixed with 1 % osmium tetroxide/1.5 % potassium
601 ferrocyanide in 0.1 M sodium cacodylate, dehydrated through ethanol and embedded in EPON (Serva)
602 using a tissue processor (Leica EM TP 709202). Ultrathin sections (80 nm) were cut using the Leica
603 uc7 ultramicrotome and collected on formvar coated cupper grids (electron microscopy sciences,
604 Hatfield, Pennsylvania). A large area scan using Scanning Transmission Detection was made using a
605 Zeiss supra55 SEM with Atlas. STEM detection with a four quadrant STEM detector was used in
606 inverted darkfield mode, at 28 kV with 30 µm aperture at 3.5 mm working distance. All images were
607 recorded at the same scan speed (cycle time 1.5 minute at 3072×2304 pixels). Contrast and brightness
608 were set based on a live histogram. High resolution large-scale STEM images at 2.5 nm pixel size
609 were generated with the external scan generator ATLAS (Fibics, Canada), individual tiles were
610 stitched in VE viewer (Fibics, Canada), exported as a html-file and uploaded to the website
611 www.nanotomy.org. Nanotomy datasets are open access available via the repository website
612 www.nanotomy.org/PW/temp02/EllenNollen.

613 ***[to be deleted] Upon acceptance of this work the website will be open access available, without***
614 ***password. Pending acceptance, the website can only be accessed by collaborators and reviewers***

615 *Cell culture*

616 Mouse embryonic fibroblasts (MEFs) were isolated from *Serf2*$^{+/+}$, *Serf2*$^{+/-}$ and *Serf2*$^{-/-}$ E13.5 embryos.
617 MEFs were cultured in T75 culture flasks (Greiner Bio-One, 658175), high–glucose Dulbecco's

618 modified Eagle's medium (Gibco), supplemented with 10% fetal bovine serum (Sigma 12133C), 1 %
619 penicillin/streptomycin (Gibco), non-essential amino acids (Gibco) and β-mercaptoethanol at 37°C, 5
620 % CO_2 and 3 % O_2. E13.5 embryos. Wild-type HEK293T and two independent clonal lines of
621 CRISPR *Serf2* KO mutant HEK 293T cells were cultured in Dulbecco's Modified Eagle Medium
622 (DMEM, Gibco; high glucose, pyruvate, 41966052), supplemented with 10 % Bovine Cow Serum
623 (BCS; Sigma 12133C) and 1 % Penicillin/Streptomycin (Gibco; 10 000 U/mL, 15140122), at 37 °C, 5
624 % CO_2. For passaging of cells, 0.05 % Trypsin-EDTA (1X), Phenol Red (Invitrogen; 25300-054) was
625 used. Regular mycoplasma tests were performed.

626 *Cell proliferation assay*

627 For the proliferation assay, 200 000 cells of each cell line were plated in triplicate in a standard 12-
628 well plate and incubated inside the IncuCyte Zoom Live-Cell Imaging System (Essen Bioscience) for
629 over 100 hours. The Incucyte system captured phase contrast images with a 10X magnification every 2
630 hours at nine distinct locations in each well to determine average confluency as a measure of cell
631 growth. The quantification was performed using the IncuCyte Zoom software. The growth experiment
632 was repeated three times. The confluency data of each experiment was normalized by min-max scaling
633 and the average of the three experiments was plotted (solid line) with the standard deviation (dashed
634 lines).

635 *Statistical analysis*

636 Unless specified otherwise, statistical analysis was performed using Graphpad v7.02. The exact
637 statistical test used for each comparison is specified in the main body of the text, together with the
638 resulting p-values. In the case of multiple comparisons, a post-hoc analysis with Bonferroni correction
639 was performed. Any corrected p-values derived from this post-hoc analysis are indicated in the text as
640 p_{bon}.

641 **Acknowledgments**

642 All LCOs were kindly provided by K. Peter R. Nilsson, Linköping University, Sweden. Part of the
643 work has been performed in the UMCG Microscopy and Imaging Center (UMIC), sponsored by
644 ZonMW grant 91111.006 and NWO 40-00506-98-9021. We thank Ben Giepmans for advise on EM
645 studies. This project was funded by a Meervoud Grant from NWO (836.09.001) (to E.A.A.N.), a
646 European Research Council (ERC) starting grant (281622 PDControl) (to E.A.A.N.), the Alumni
647 chapter Gooische Groningers facilitated by the Ubbo Emmius Fonds (to E.A.A.N), an Aspasia
648 fellowship from NWO (015.014.005) (to E.A.A.N.).

649 **Conflict of Interests**

650 The authors declare that they have no conflict of interest.

651 **References**

652 Borchelt DR, Thinakaran G, Eckman CB, Lee MK, Davenport F, Ratovitsky T, Prada CM, Kim G,
653 Seekins S, Yager D, *et al* (1996) Familial Alzheimer's disease-linked presenilin I variants elevate
654 aβ1- 42/1-40 ratio in vitro and in vivo. *Neuron*

655 Bousset L, Pieri L, Ruiz-Arlandis G, Gath J, Jensen PH, Habenstein B, Madiona K, Olieric V,
656 Böckmann A, Meier BH, *et al* (2013) Structural and functional characterization of two alpha-
657 synuclein strains. *Nat Commun* 4: 2575

658 Bugiani O, Giaccone G, Rossi G, Mangieri M, Capobianco R, Morbin M, Mazzoleni G, Cupidi C,
659 Marcon G, Giovagnoli A, *et al* (2010) Hereditary Cerebral Hemorrhage With Amyloidosis
660 Associated With the E693K Mutation of APP. *Arch Neurol* 67: 987–995

661 Chartier-Harlin M-C, Crawford F, Houlden H, Warren A, Hughes D, Fidani L, Goate A, Rossor M,
662 Roques P, Hardy J, *et al* (1991) Early-onset Alzheimer's disease caused by mutations at codon
663 717 of the β-amyloid precursor protein gene. *Nature* 353: 844–846

664 Choi W, Zibaee S, Jakes R, Serpell LC, Davletov B, Anthony Crowther R & Goedert M (2004)
665 Mutation E46K increases phospholipid binding and assembly into filaments of human α-
666 synuclein. *FEBS Lett* 576: 363–368

667 Ciemerych MA & Sicinski P (2005) Cell cycle in mouse development. *Oncogene*
668 doi:10.1038/sj.onc.1208608 [PREPRINT]

669 Citron M, Oltersdorf T, Haass C, McConlogue L, Hung AY, Seubert P, Vigo-Pelfrey C, Lieberburg I
670 & Selkoe DJ (1992) Mutation of the β-amyloid precursor protein in familial Alzheimer's disease
671 increases β-protein production. *Nature*

672 Citron M, Westaway D, Xia W, Carlson G, Diehl T, Levesque G, Johnson-Wood K, Lee M, Seubert P,
673 Davis A, *et al* (1997) Mutant presenilins of Alzheimer's disease increase production of 42-

674 residue amyloid beta-protein in both transfected cells and transgenic mice. *Nat Med* 3: 67–72

675 Cohen E, Paulsson JF, Blinder P, Burstyn-Cohen T, Du D, Estepa G, Adame A, Pham HM,
676 Holzenberger M, Kelly JW, *et al* (2009) Reduced IGF-1 Signaling Delays Age-Associated
677 Proteotoxicity in Mice. *Cell* 139: 1157–1169

678 Cohen ML, Kim C, Haldiman T, ElHag M, Mehndiratta P, Pichet T, Lissemore F, Shea M, Cohen Y,
679 Chen W, *et al* (2015) Rapidly progressive Alzheimer's disease features distinct structures of
680 amyloid-β. *Brain* 138: 1009–1022

681 Conway KA, Harper JD & Lansbury PT (1998) Accelerated in vitro fibril formation by a mutant α-
682 synuclein linked to early-onset Parkinson disease. *Nat Med*

683 Conway KA, Lee SJ, Rochet JC, Ding TT, Williamson RE & Lansbury PT (2000) Acceleration of
684 oligomerization, not fibrillization, is a shared property of both α-synuclein mutations linked to
685 early-onset Parkinson's disease: Implications for pathogenesis and therapy. *Proc Natl Acad Sci U*
686 *S A*

687 Cooper JK, Schilling G, Peters MF, Herring WJ, Sharp AH, Kaminsky Z, Masone J, Khan FA,
688 Delanoy M, Borchelt DR, *et al* (1998) Truncated N-terminal fragments of huntingtin with
689 expanded glutamine repeats form nuclear and cytoplasmic aggregates in cell culture. *Hum Mol*
690 *Genet*

691 Cruts M, Dermaut B, Rademakers R, Van Den Broeck M, Stögbauer F & Van Broeckhoven C (2003)
692 Novel APP mutation V715A associated with presenile Alzheimer's disease in a German family.
693 *J Neurol* 250: 1374–1375

694 Duff K, Eckman C, Zehr C, Yu X, Prada CM, Perez-Tur J, Hutton M, Buee L, Harigaya Y, Yager D,
695 *et al* (1996) Increased amyloid-β42(43) in brains of mice expressing mutant presenilin 1. *Nature*

696 Eckman CB, Mehta ND, Crook R, Perez-tur J, Prihar G, Pfeiffer E, Graff-Radford N, Hinder P, Yager

697 D, Zenk B, *et al* (1997) A new pathogenic mutation in the APP gene (I716V) increases the
698 relative proportion of A beta 42(43). *Hum Mol Genet* 6: 2087–9

699 Elkins MR, Wang T, Nick M, Jo H, Lemmin T, Prusiner SB, Degrado WF, Stö Hr J & Hong M (2016)
700 Structural Polymorphism of Alzheimer's β-Amyloid Fibrils as Controlled by an E22 Switch: A
701 Solid-State NMR Study.

702 Falsone SF, Meyer NH, Schrank E, Leitinger G, Pham CLL, Fodero-Tavoletti MT, Holmberg M,
703 Dulle M, Scicluna B, Gesslbauer B, *et al* (2012) SERF Protein Is a Direct Modifier of Amyloid
704 Fiber Assembly. *Cell Rep* 2: 358–371

705 Gath J, Bousset L, Habenstein B, Melki R, Böckmann A & Meier BH (2014) Unlike Twins: An NMR
706 Comparison of Two α-Synuclein Polymorphs Featuring Different Toxicity. *PLoS One* 9: e90659

707 Ghosh D, Mondal M, Mohite GM, Singh PK, Ranjan P, Anoop A, Ghosh S, Jha NN, Kumar A & Maji
708 SK (2013) The Parkinson's Disease-Associated H50Q Mutation Accelerates α-Synuclein
709 Aggregation *in Vitro*. *Biochemistry* 52: 6925–6927

710 Ghosh D, Sahay S, Ranjan P, Salot S, Mohite GM, Singh PK, Dwivedi S, Carvalho E, Banerjee R,
711 Kumar A, *et al* (2014) The Newly Discovered Parkinson's Disease Associated Finnish Mutation
712 (A53E) Attenuates α-Synuclein Aggregation and Membrane Binding. *Biochemistry* 53: 6419–
713 6421

714 Glenner GG & Wong CW (1984) Alzheimer's disease: Initial report of the purification and
715 characterization of a novel cerebrovascular amyloid protein. *Biochem Biophys Res Commun*

716 Goate A, Chartier-Harlin MC, Mullan M, Brown J, Crawford F, Fidani L, Giuffra L, Haynes A, Irving
717 N, James L, *et al* (1991) Segregation of a missense mutation in the amyloid precursor protein
718 gene with familial Alzheimer's disease. *Nature* 349: 704–706

719 Grabowski TJ, Cho HS, Vonsattel JPG, Rebeck GW & Greenberg SM (2001) Novel amyloid

720 precursor protein mutation in an Iowa family with dementia and severe cerebral amyloid
721 angiopathy. *Ann Neurol* 49: 697–705

722 Grant MA, Lazo ND, Lomakin A, Condron MM, Arai H, Yamin G, Rigby AC & Teplow DB (2007)
723 Familial Alzheimer's disease mutations alter the stability of the amyloid-protein monomer
724 folding nucleus

725 Grundke-Iqbal I, Iqbal K, Quinlan M, Tung YC, Zaidi MS & Wisniewski HM (1986a) Microtubule-
726 associated protein tau. A component of Alzheimer paired helical filaments. *J Biol Chem* 261:
727 6084–6089

728 Grundke-Iqbal I, Iqbal K, Tung Y-C, Quinlan M, Wisniewski HM & Bindert LI (1986b) Abnormal
729 phosphorylation of the microtubule-associated protein tau (tau) in Alzheimer cytoskeletal
730 pathology. *Proc Natl Acad Sci U S A* 83: 4913–4917

731 Guerreiro RJ, Baquero M, Blesa R, Boada M, Brás JM, Bullido MJ, Calado A, Crook R, Ferreira C,
732 Frank A, *et al* (2010) Genetic screening of Alzheimer's disease genes in Iberian and African
733 samples yields novel mutations in presenilins and APP. *Neurobiol Aging* 31: 725–731

734 Guerrero-Ferreira R, Taylor NMI, Arteni A-A, Kumari P, Mona D, Ringler P, Britschgi M, Lauer ME,
735 Verasdock J, Riek R, *et al* (2019) Two new polymorphic structures of alpha-synuclein solved by
736 cryo-electron microscopy. *bioRxiv*: 654582

737 Haass C, Lemere CA, Capell A, Citron M, Seubert P, Schenk D, Lannfelt L & Selkoe DJ (1995) The
738 Swedish mutation causes early-onset Alzheimer's disease by beta-secretase cleavage within the
739 secretory pathway. *Nat Med* 1: 1291–6

740 van Ham TJ, Holmberg MA, van der Goot AT, Teuling E, Garcia-Arencibia M, Kim H eui, Du D,
741 Thijssen KL, Wiersma M, Burggraaff R, *et al* (2010) Identification of MOAG-4/SERF as a
742 regulator of age-related proteotoxicity. *Cell* 142: 601–612

743 Heise H, Celej MS, Becker S, Riedel D, Pelah A, Kumar A, Jovin TM & Baldus M (2008) Solid-State
744 NMR Reveals Structural Differences between Fibrils of Wild-Type and Disease-Related A53T
745 Mutant α-Synuclein. *J Mol Biol* 380: 444–450

746 Huang DW, Sherman BT & Lempicki RA (2009a) Bioinformatics enrichment tools: paths toward the
747 comprehensive functional analysis of large gene lists. *Nucleic Acids Res* 37: 1–13

748 Huang DW, Sherman BT & Lempicki RA (2009b) Systematic and integrative analysis of large gene
749 lists using DAVID bioinformatics resources. *Nat Protoc* 4: 44–57

750 Huang Y, Skwarek-Maruszewska A, Horré K, Vandewyer E, Wolfs L, Snellinx A, Saito T, Radaelli E,
751 Corthout N, Colombelli J, *et al* (2015) Loss of GPR3 reduces the amyloid plaque burden and
752 improves memory in Alzheimer's disease mouse models. *Sci Transl Med* 7: 309ra164

753 Inayathullah M & Teplow DB (2011) Structural dynamics of the Δe22 (Osaka) familial Alzheimer's
754 disease-linked amyloid β-protein. *Amyloid* 18: 98–107

755 Kaufman MH (1992) The Atlas of Mouse Development Elsevier Science

756 Kaufman MH & Bard JBL (1999) The Anatomical Basis of Mouse Development Elsevier Science

757 Klingstedt T, Aslund A, Simon RA, Johansson LBG, Mason JJ, Nyström S, Hammarström P &
758 Nilsson KPR (2011) Synthesis of a library of oligothiophenes and their utilization as fluorescent
759 ligands for spectral assignment of protein aggregates. *Org Biomol Chem* 9: 8356–70

760 Kulic L, McAfoose J, Welt T, Tackenberg C, Späni C, Wirth F, Finder V, Konietzko U, Giese M,
761 Eckert A, *et al* (2012) Early accumulation of intracellular fibrillar oligomers and late congophilic
762 amyloid angiopathy in mice expressing the Osaka intra-Aβ APP mutation. *Transl Psychiatry* 2:
763 e183–e183

764 Kumar-Singh S, De Jonghe C, Cruts M, Kleinert R, Wang R, Mercken M, De Strooper B,

765 Vanderstichele H, Löfgren A, Vanderhoeven I, *et al* (2000) Nonfibrillar diffuse amyloid
766 deposition due to a gamma(42)-secretase site mutation points to an essential role for N-truncated
767 A beta(42) in Alzheimer's disease. *Hum Mol Genet* 9: 2589–98

768 Kumar-Singh S, Theuns J, Van Broeck B, Pirici D, Vennekens K, Corsmit E, Cruts M, Dermaut B,
769 Wang R & Van Broeckhoven C (2006) Mean age-of-onset of familial Alzheimer disease caused
770 by presenilin mutations correlates with both increased Aβ42 and decreased Aβ40. *Hum Mutat*

771 Langley CH & Charlesworth B (1997) Nature © Macmillan Publishers Ltd 1997 expansion of
772 xenotransplantation

773 Lazo ND, Grant MA, Condron MC, Rigby AC & Teplow DB (2009) On the nucleation of amyloid β-
774 protein monomer folding. *Protein Sci* 14: 1581–1596

775 Lemere CA, Lopera F, Kosik KS, Lendon CL, Ossa J, Saido TC, Yamaguchi H, Ruiz A, Martinez A,
776 Madrigal L, *et al* (1996) The E280A presenilin 1 Alzheimer mutation produces increased A beta
777 42 deposition and severe cerebellar pathology. *Nat Med* 2: 1146–50

778 Leung AKL, Gerlich D, Miller G, Lyon C, Lam YW, Lleres D, Daigle N, Zomerdijk J, Ellenberg J &
779 Lamond AI (2004) Quantitative kinetic analysis of nucleolar breakdown and reassembly during
780 mitosis in live human cells. *J Cell Biol* 166: 787–800

781 Li B, Ge P, Murray KA, Sheth P, Zhang M, Nair G, Sawaya MR, Shin WS, Boyer DR, Ye S, *et al*
782 (2018) Cryo-EM of full-length α-synuclein reveals fibril polymorphs with a common structural
783 kernel. *Nat Commun* 9: 3609

784 Lord A, Kalimo H, Eckman C, Zhang X-Q, Lannfelt L & Nilsson LNG (2006) The Arctic Alzheimer
785 mutation facilitates early intraneuronal Aβ aggregation and senile plaque formation in transgenic
786 mice. *Neurobiol Aging* 27: 67–77

787 Lord A, Philipson O, Klingstedt T, Westermark G, Hammarström P, Nilsson KPR & Nilsson LNG

788 (2011) Observations in APP bitransgenic mice suggest that diffuse and compact plaques form via
789 independent processes in Alzheimer's disease. *Am J Pathol* 178: 2286–2298

790 Lu JX, Qiang W, Yau WM, Schwieters CD, Meredith SC & Tycko R (2013) Molecular structure of β-
791 amyloid fibrils in alzheimer's disease brain tissue. *Cell*

792 Masters CL, Simms G, Weinman NA, Multhaupt G, Mcdonald BL & Beyreuthert K (1985) Amyloid
793 plaque core protein in Alzheimer disease and Down syndrome. *Proc Natl Acad Sci U S A* 82:
794 4245–4249

795 Meinen BA, Gadkari V V., Stull F, Ruotolo BT & Bardwell JCA (2019) SERF engages in a fuzzy
796 complex that accelerates primary nucleation of amyloid proteins. *Proc Natl Acad Sci*

797 Merle DA, Witternigg A, Tam-Amersdorfer C, Hartlmüller C, Spreitzer E, Schrank E, Wagner-
798 Lichtenegger S, Werzer O, Zangger K, Kungl AJ, *et al* (2019) Increased Aggregation Tendency
799 of Alpha-Synuclein in a Fully Disordered Protein Complex. *J Mol Biol* 431: 2581–2598

800 Meyer NH, Dellago H, Tam-Amersdorfer C, Merle DA, Parlato R, Gesslbauer B, Almer J,
801 Gschwandtner M, Leon A, Franzmann TM, *et al* (2019) Structural fuzziness of the RNA-
802 organizing protein SERF1a determines a toxic gain-of-interaction. *bioRxiv*: 713511

803 Miravalle L, Tokuda T, Chiarle R, Giaccone G, Bugiani O, Tagliavini F, Frangione B & Ghiso J
804 (2000) Substitutions at Codon 22 of Alzheimer's A Peptide Induce Diverse Conformational
805 Changes and Apoptotic Effects in Human Cerebral Endothelial Cells*.

806 Müller U, Winter P, Bolender C & Nolte D (2014) Previously Unrecognized Missense Mutation
807 E126K of PSEN2 Segregates with Early Onset Alzheimer's Disease in a Family. *J Alzheimer's*
808 *Dis* 42: 109–113

809 Murayama O, Tomita T, Nihonmatsu N, Murayama M, Sun X, Honda T, Iwatsubo T & Takashima A
810 (1999) Enhancement of amyloid β 42 secretion by 28 different presenilin 1 mutations of familial

811 Alzheimer's disease. *Neurosci Lett* 265: 61–63

812 Murray SA, Morgan JL, Kane C, Sharma Y, Heffner CS, Lake J & Donahue LR (2010) Mouse
813 Gestation Length Is Genetically Determined. *PLoS One* 5: e12418

814 Murrell JR, Hake AM, Quaid KA, Farlow MR & Ghetti B (2000) Early-Onset Alzheimer Disease
815 Caused by a New Mutation (V717L) in the Amyloid Precursor Protein Gene. *Arch Neurol* 57:
816 885

817 Narhi L, Wood SJ, Steavenson S, Jiang Y, Wu GM, Anafi D, Kaufman SA, Martin F, Sitney K, Denis
818 P, *et al* (1999) Both Familial Parkinson's Disease Mutations Accelerate α-Synuclein
819 Aggregation. *J Biol Chem* 274: 9843–9846

820 Nekooki-Machida Y, Kurosawa M, Nukina N, Ito K, Oda T & Tanaka M (2009) Distinct
821 conformations of in vitro and in vivo amyloids of huntingtin-exon1 show different cytotoxicity.
822 *Proc Natl Acad Sci U S A* 106: 9679–84

823 Ni C-L, Shi H-P, Yu H-M, Chang Y-C & Chen Y-R (2011) Folding stability of amyloid-β 40
824 monomer is an important determinant of the nucleation kinetics in fibrillization. *FASEB J* 25:
825 1390–1401

826 Nilsberth C, Westlind-Danielsson A, Eckman CB, Condron MM, Axelman K, Forsell C, Stenh C,
827 Luthman J, Teplow DB, Younkin SG, *et al* (2001) The 'Arctic' APP mutation (E693G) causes
828 Alzheimer's disease by enhanced Aβ protofibril formation. *Nat Neurosci* 4: 887–893

829 Van Nostrand WE, Melchor JP, Cho HS, Greenberg SM & Rebeck GW (2001) Pathogenic effects of
830 D23N Iowa mutant amyloid beta -protein. *J Biol Chem* 276: 32860–6

831 Nyström S, Psonka-Antonczyk KM, Ellingsen PG, Johansson LBG, Reitan N, Handrick S, Prokop S,
832 Heppner FL, Wegenast-Braun BM, Jucker M, *et al* (2013) Evidence for Age-Dependent in Vivo
833 Conformational Rearrangement within Aβ Amyloid Deposits. *ACS Chem Biol* 8: 1128–1133

834 Ovchinnikova OY, Finder VH, Vodopivec I, Nitsch RM & Glockshuber R (2011) The Osaka FAD
835 Mutation E22Δ Leads to the Formation of a Previously Unknown Type of Amyloid β Fibrils and
836 Modulates Aβ Neurotoxicity. *J Mol Biol* 408: 780–791

837 Petkova AT, Leapman RD, Guo Z, Yau WM, Mattson MP & Tycko R (2005) Self-propagating,
838 molecular-level polymorphism in Alzheimer's β-amyloid fibrils. *Science (80-)*

839 Pevny LH, Sockanathan S, Placzek M & Lovell-Badge R (1998) A role for SOX1 in neural
840 determination. *Development*

841 Philipson O, Hammarström P, Nilsson KPR, Portelius E, Olofsson T, Ingelsson M, Hyman BT,
842 Blennow K, Lannfelt L, Kalimo H, *et al* (2009) A highly insoluble state of Aβ similar to that of
843 Alzheimer's disease brain is found in Arctic APP transgenic mice. *Neurobiol Aging* 30: 1393–
844 1405

845 Philipson O, Lord A, Lalowski M, Soliymani R, Baumann M, Thyberg J, Bogdanovic N, Olofsson T,
846 Tjernberg LO, Ingelsson M, *et al* (2012) The Arctic amyloid-β precursor protein (AβPP)
847 mutation results in distinct plaques and accumulation of N- and C-truncated Aβ. *Neurobiol Aging*
848 33: 1010.e1-1010.e13

849 Pras A, Houben B, Aprile FA, Seinstra R, Gallardo R, Janssen L, Hogewerf W, De Vleeschouwer M,
850 Mata-Cabana A, Koopman M, *et al* (2020) The cellular modifier MOAG-4/SERF drives amyloid
851 formation through charge complementation. *bioRxiv*: 2020.12.09.417709

852 Psonka-Antonczyk KM, Hammarström P, Johansson LBG, Lindgren M, Stokke BT, Nilsson KPR &
853 Nyström S (2016) Nanoscale Structure and Spectroscopic Probing of Aβ1-40 Fibril Bundle
854 Formation. *Front Chem*

855 Qiang W, Yau W-M, Lu J-X, Collinge J & Tycko R (2017) Structural variation in amyloid-β fibrils
856 from Alzheimer's disease clinical subtypes. *Nature* 541: 217–221

857 Radde R, Bolmont T, Kaeser S a, Coomaraswamy J, Lindau D, Stoltze L, Calhoun ME, Jäggi F,
858 Wolburg H, Gengler S, *et al* (2006) Abeta42-driven cerebral amyloidosis in transgenic mice
859 reveals early and robust pathology. *EMBO Rep* 7: 940–6

860 Rasmussen J, Mahler J, Beschorner N, Kaeser SA, Häsler LM, Baumann F, Nyström S, Portelius E,
861 Blennow K, Lashley T, *et al* (2017) Amyloid polymorphisms constitute distinct clouds of
862 conformational variants in different etiological subtypes of Alzheimer's disease. *Proc Natl Acad*
863 *Sci* 114: 13018–13023

864 Rogaev EI, Sherrington R, Rogaeva EA, Levesque G, Ikeda M, Liang Y, Chi H, Lin C, Holman K,
865 Tsuda T, *et al* (1995) Familial Alzheimer's disease in kindreds with missense mutations in a gene
866 on chromosome 1 related to the Alzheimer's disease type 3 gene. *Nature* 376: 775–778

867 Schellenberg G, Bird T, Wijsman E, Orr H, Anderson L, Nemens E, White J, Bonnycastle L, Weber J,
868 Alonso M, *et al* (1992) Genetic linkage evidence for a familial Alzheimer's disease locus on
869 chromosome 14. *Science (80-)* 258: 668–671

870 Scherzinger E, Sittler A, Schweiger K, Heiser V, Lurz R, Hasenbank R, Bates GP, Lehrach H &
871 Wanker EE (1999) Self-assembly of polyglutamine-containing huntingtin fragments into
872 amyloid-like fibrils: Implications for Huntington's disease pathology (huntingtinglutamine
873 repeataggregation)

874 Schindelin J, Arganda-Carreras I, Frise E, Kaynig V, Longair M, Pietzsch T, Preibisch S, Rueden C,
875 Saalfeld S, Schmid B, *et al* (2012) Fiji: an open-source platform for biological-image analysis.
876 *Nat Methods* 9: 676–682

877 Sherrington R, Rogaev EI, Liang Y, Rogaeva EA, Levesque G, Ikeda M, Chi H, Lin C, Li G, Holman
878 K, *et al* (1995) Cloning of a gene bearing missense mutations in early-onset familial Alzheimer's
879 disease. *Nature* 375: 754–760

880 Shimada H, Ataka S, Tomiyama T, Takechi H, Mori H & Miki T (2011) Clinical course of patients
881 with familial early-onset Alzheimer's disease potentially lacking senile plaques bearing the
882 E693Δ mutation in amyloid precursor protein. *Dement Geriatr Cogn Disord* 32: 45–54

883 Skarnes WC, Rosen B, West AP, Koutsourakis M, Bushell W, Iyer V, Mujica AO, Thomas M,
884 Harrow J, Cox T, *et al* (2011) A conditional knockout resource for the genome-wide study of
885 mouse gene function. *Nature* 474: 337–342

886 Sun C-S, Lee C-C, Li Y-N, Yao-Chen Yang S, Lin C-H, Chang Y-C, Liu P-F, He R-Y, Wang C-H,
887 Chen W, *et al* (2015) Conformational switch of polyglutamine-expanded huntingtin into benign
888 aggregates leads to neuroprotective effect. *Sci Rep* 5: 14992

889 Suzuki N, Cheung TT, Cai XD, Odaka A, Otvos L, Eckman C, Golde TE & Younkin SG (1994) An
890 increased percentage of long amyloid β protein secreted by familial amyloid β protein precursor
891 (βAPP717) mutants. *Science (80-)*

892 Takashima Y, Era T, Nakao K, Kondo S, Kasuga M, Smith AG & Nishikawa S-I (2007)
893 Neuroepithelial Cells Supply an Initial Transient Wave of MSC Differentiation. *Cell* 129: 1377–
894 1388

895 Tomiyama T, Matsuyama S, Iso H, Umeda T, Takuma H, Ohnishi K, Ishibashi K, Teraoka R, Sakama
896 N, Yamashita T, *et al* (2010) A Mouse Model of Amyloid β Oligomers: Their Contribution to
897 Synaptic Alteration, Abnormal Tau Phosphorylation, Glial Activation, and Neuronal Loss In
898 Vivo. *J Neurosci* 30: 4845–4856

899 Tomiyama T, Nagata T, Shimada H, Teraoka R, Fukushima A, Kanemitsu H, Takuma H, Kuwano R,
900 Imagawa M, Ataka S, *et al* (2008) A new amyloid β variant favoring oligomerization in
901 Alzheimer's-type dementia. *Ann Neurol* 63: 377–387

902 Visintin R & Amon A (2000) The nucleolus: the magician's hat for cell cycle tricks. *Curr Opin Cell*

903 *Biol* 12: 372–377

904 Ward JM, Elmore SA & Foley JF (2012) Pathology Methods for the Evaluation of Embryonic and
905 Perinatal Developmental Defects and Lethality in Genetically Engineered Mice. *Vet Pathol* 49:
906 71–84

907 Wood HB & Episkopou V (1999) Comparative expression of the mouse Sox1, Sox2 and Sox3 genes
908 from pre-gastrulation to early somite stages. *Mech Dev*

909 Yoshimura Y, Holmberg MA, Kukic P, Andersen CB, Mata-Cabana A, Falsone SF, Vendruscolo M,
910 Nollen EAA & Mulder FAA (2017) MOAG-4 promotes the aggregation of α-synuclein by
911 competing with self-protective electrostatic interactions. *J Biol Chem* 292: 8269–8278

912

913 **Figure legends**

914 **Figure 1. Full-body *Serf2*$^{-/-}$ mice display a developmental delay and perinatal lethality. (A)**
915 Schematic overview of the crossing scheme with full-body *Serf2*$^{+/-}$ mice and the resulting genotypic
916 composition of the offspring at embryonic and postnatal stage. **(B)** Absolute animal counts for the
917 three genotypes in the offspring at various days of embryonic development(E13.5, E15.5 and E17.5),
918 at birth (P0) and at time of weaning (P22). **(C)** Real time RT-PCR analyses of *Serf1* and *Serf2* RNA
919 levels in E13.5 heads normalized to housekeeping gene beta-actin (n=4/group, mean±SD, One-way
920 ANOVA for each gene, Bonferroni corrected post-hoc comparison between genotypes ***p<0.001).
921 **(D)** Western blot of SERF2 and actin in *Serf2*$^{+/+}$, *Serf2*$^{+/-}$, *Serf2*$^{-/-}$embryos at E13.5 (black arrow
922 indicates SERF2 band). **(E)** Length measurements of *Serf2*$^{+/+}$, *Serf2*$^{+/-}$, *Serf2*$^{-/-}$ embryos at E15.5, E17.5
923 and P0 (black line = mean, Two-way ANOVA with factors age and genotype, Bonferroni corrected
924 post-hoc comparison for *Serf2*$^{+/-}$ and *Serf2*$^{-/-}$ compared to *Serf2*$^{-/-}$ *p<0.05; ***p<0.001). **(F)**
925 Hematoxylin and eosin stained lung tissue from *Serf2*$^{+/+}$ and *Serf2*$^{-/-}$ pups at P0 (top: *Serf2*$^{-/-}$, bottom:
926 *Serf2*$^{+/+}$, scale bar=500µm, rectangle =5x magnification in right picture, **(G)** Quantification of the
927 saccolar space in lung tissue from *Serf2*$^{+/+}$ and *Serf2*$^{-/-}$ pups at P0 (black line = mean, t-test **p<0.01).
928 For all mouse data panels: *Serf2*$^{+/+}$= black, *Serf2*$^{+/-}$ = dark grey, *Serf2*$^{-/-}$ = light grey.

929 **Figure 2. Crossing a conditional *Serf2* KO with an AM background does not affect the overall**
930 **levels of APP and Aβ. (A)** Schematic overview of the cross between brain-specific *Serf2* KO mice
931 and the amyloid model resulting in four experimental groups: WT, *Serf2*$^{br-/-}$, AM and AM;*Serf2*$^{br-/-}$.
932 **(B)** Timeline for the Aβ pathology in the amyloid model and the selected time points for this study.
933 **(C)** Real time RT-PCR analyses of *Serf2* RNA levels in the brain tissue of all experimental groups at 1
934 and 3 months of age normalized to housekeeping gene beta-actin (n=6/group, mean±SD, Two-way
935 ANOVA with factors age and genotype, Bonferroni corrected post-hoc for individual groups
936 compared to WT). **(D)** Western blot of SERF2 and actin in brain tissue of all experimental groups at 1
937 and 3 months of age. **(E)** Brain weight of all experimental groups at 1 and 3 months of age (black line
938 = mean, Two-way ANOVA with factors age and genotype, Bonferroni corrected post-hoc for

939 individual groups compared to WT). **(F)** Brain weight of unfloxed control groups at 3 months of age
940 (black line = mean, One-way ANOVA, Bonferroni corrected post-hoc for individual groups compared
941 to WT). **(G)** Number of cortical nuclei per mm^2 in hematoxylin and eosin stained brain tissue of all
942 experimental groups at 3 months of age. (n=3/group, mean±SD, Kruskal-Wallis p=0.5566). **(H)** Real
943 time RT-PCR analyses of APP RNA levels in the brain tissue of AM and AM;*Serf2*$^{br-/-}$ mice at 1 and 3
944 months of age normalized to housekeeping gene beta-actin (n=6/group, mean±SD, t-test between
945 genotypes at both ages not significant). **(I)** Western blot of APP and beta-actin in brain tissue of AM
946 and AM;*Serf2*$^{br-/-}$ mice at 3 months of age versus 1-month-old non-AM controls. **(J)** Quantification of
947 total APP protein levels in brains of AM and AM;*Serf2*$^{br-/-}$ mice at 1 and 3 months of age normalized
948 to beta-actin levels. (black line = mean, t-test between genotypes at both ages not significant). **(K)**
949 $A\beta_{40}$ and **(L)** $A\beta_{42}$ levels in brain lysate from AM and AM;*Serf2*$^{br-/-}$ mice at 1 and 3 months of age as
950 determined by ELISA normalized to total protein content. (black line = mean, t-test between
951 genotypes at both ages not significant). **(M)** Correlation plot depicting the relationship between $A\beta_{40}$
952 and $A\beta_{42}$ levels in AM (black) and AM;*Serf2*$^{br-/-}$ (grey) mice at 3 months of age (detailed statistics in
953 Supplemental Table 3). In panels A-L: WT = black, *Serf2*$^{br-/-}$ = light grey , AM = dark grey and
954 AM;*Serf2*$^{br-/-}$ = white; ***p<0.001; **p<0.01.

955 **Figure 3. Brain-specific *Serf2* KO display increased Aβ deposition and amyloid .(A)** Detailed light
956 microscope images of the 6E10-stained cortical region marked on the sagittal section in Supplemental
957 Figure 5 from 3-month-old AM and AM;*Serf2*$^{br-/-}$ mice (scale bar = 100μm). **(B)** Quantification of the
958 Aβ deposits in the region of interest (ROI) of 6E10 immunostained sagittal brain sections from 1- and
959 3-month-old AM and AM;*Serf2*$^{br-/-}$ mice (black line = mean, One-way ANOVA between genotypes at
960 both ages, Bonferroni corrected post-hoc between AM and AM;*Serf2*$^{br-/-}$ not significant). **(C)**
961 Correlation plot depicting the relationship between $A\beta_{40}$ levels and 6E10 plaque density in AM (black)
962 and AM;*Serf2*$^{br-/-}$ (grey) mice at 3 months of age. **(D)** Correlation plot depicting the relationship
963 between $A\beta_{42}$ levels and 6E10 plaque density in AM (black) and AM;*Serf2*$^{br-/-}$ (grey) mice at 3 months
964 of age. **(E)** Quantification of the Aβ deposits in the ROI of W0-2 immunostained sagittal brain
965 sections from 1- and 3-month-old AM and AM;*Serf2*$^{br-/-}$ mice (black line = mean, One-way ANOVA

966 between genotypes at both ages, Bonferroni corrected post-hoc between AM and AM;*Serf2*$^{br-/-}$ not
967 significant). **(F)** Correlation plot depicting the relationship between 6E10 deposits and W0-2 deposits
968 in AM (black) and AM;*Serf2*$^{br-/-}$ (grey) mice at 3 months of age. **(G)** Quantification of the plaque
969 density in the ROI of Thioflavin-S stained sagittal brain sections from 1- and 3-month-old AM and
970 AM;*Serf2*$^{br-/-}$ mice (black line = mean, One-way ANOVA between genotypes at both ages, Bonferroni
971 corrected post-hoc between AM and AM;*Serf2*$^{br-/-}$ not significant). **(H)** Correlation plot depicting the
972 relationship between Aβ_{40} levels and ThS plaque density in AM (black) and AM;*Serf2*$^{br-/-}$ (grey) mice
973 at 3 months of age. **(I)** Correlation plot depicting the relationship between Aβ_{42} levels and ThS plaque
974 density in AM (black) and AM;*Serf2*$^{br-/-}$ (grey) mice at 3 months of age. **(I)** Correlation plot depicting
975 the relationship between 6E10 deposits and ThS plaques in AM (black) and AM;*Serf2*$^{br-/-}$ (grey) mice
976 at 3 months of age. In all panels ROI = cortical and hippocampal area; In panels B,E and G: WT =
977 black, *Serf2*$^{br-/-}$ = light grey , AM = dark grey and AM;*Serf2*$^{br-/-}$ = white; for correlation plots: detailed
978 statistics in Supplemental Table 3; ***p<0.001; **p<0.01; *p <0.05.

979 **Figure 4. Brain-specific *Serf2* KO alters the structural composition of amyloid plaques. (A)**
980 Graph showing the theoretical LCO dye emission spectra for qFTAA, which binds mature Aβ fibrils
981 (blue), and hFTAA, which binds both mature fibrils and prefibrillar Aβ species (red). **(B)** Frequency
982 distribution of the ratio in fluorescence intensity at 502 nm and 588 nm for all amyloid plaques
983 identified by confocal microscopy in AM (blue) and AM;*Serf2*$^{br-/-}$ (red) mice at 3 months of age. Three
984 peak frequency categories were identified: low IR(red), medium IR (green) and high IR (blue) (n=6
985 mice/genotype). **(C)** Dot plot representing the intensity ratio of all amyloid plaques identified by
986 confocal microscopy for AM and AM;*Serf2*$^{br-/-}$ mice at 3 months of age (colors represent the IR
987 categories defined in panel B, black circles correspond to the plaques depicted in panel E, black line =
988 mean, t-test ***p<0.001) (n=6 mice/genotype). **(D)** Correlation plot depicting the relationship between
989 6E10 plaque density in the ROI and the LCO average intensity ratio in AM (black) and AM;*Serf2*$^{br-/-}$
990 (grey) mice at 3 months of age (ROI = cortical and hippocampal area, detailed statistics in
991 Supplemental Table 3). **(E)** Spectral confocal microscopy images of amyloid plaques in AM and
992 AM;*Serf2*$^{br-/-}$ mice at 3 months of age of double stained with qFTAA and hFTAA (top= fluorescence

993 at 502 nm, middle= fluorescence at 588 nm, bottom=merged image of 502 nm and 588 nm
994 fluorescence, scale bar = 5 μm). **(F)** Scanning transmission electron microscopy pictures of amyloid
995 plaques in the cortex of AM and AM;*Serf2*$^{br-/-}$ mice at 3 months of age (top scale bar 5μm, rectangle =
996 zoomed region in bottom picture, bottom scale bar = 1μm). High-resolution EM images are available
997 via http://www.nanotomy.org.

Figure 1

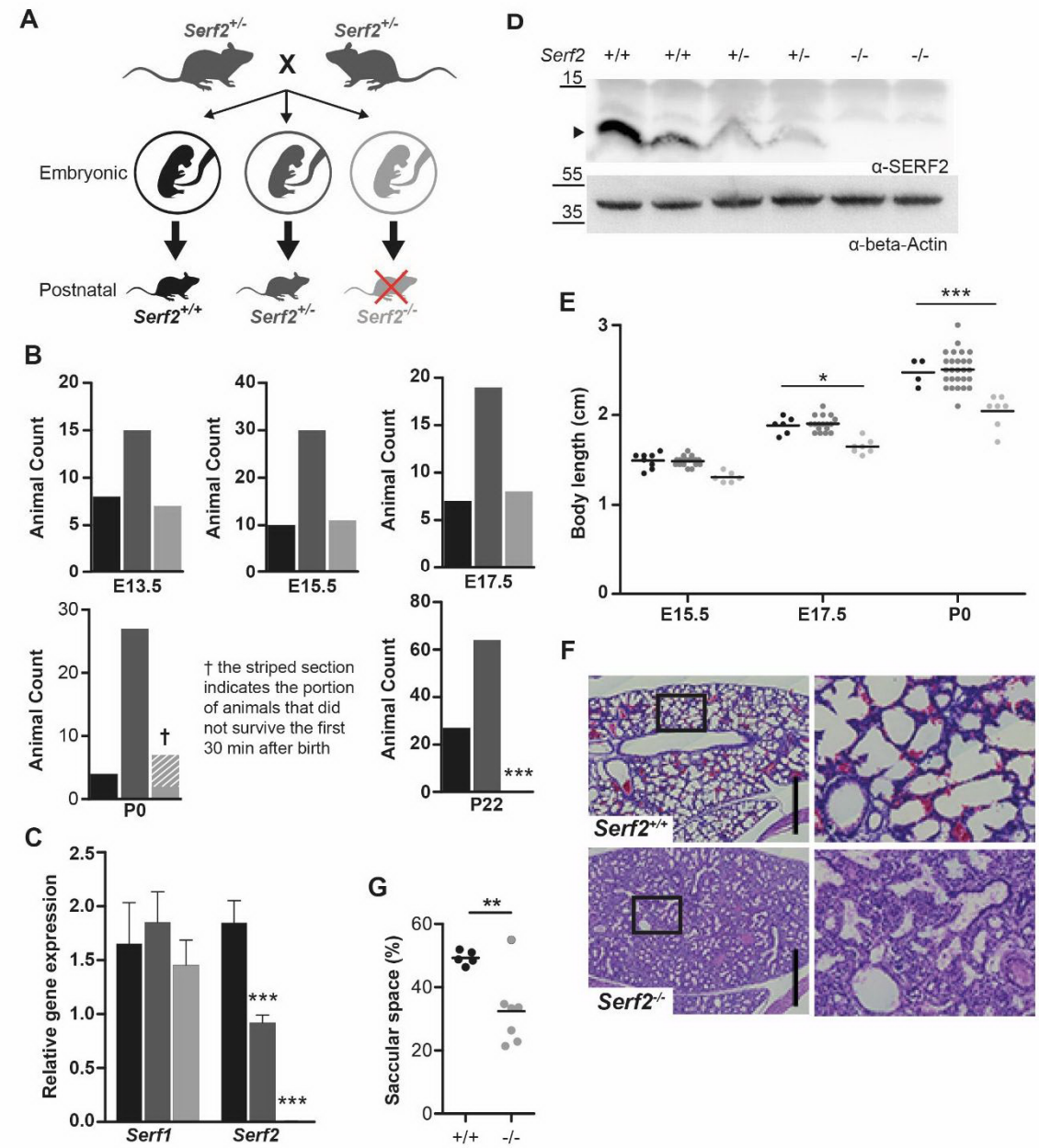
A
Serf2+/-
X
Serf2+/-
Embryonic
Postnatal
Serf2+/+
Serf2+/-
Serf2-/-
B
Animal Count
E13.5
E15.5
E17.5
P0
P22
† the striped section indicates the portion of animals that did not survive the first 30 min after birth
C
Relative gene expression
Serf1
Serf2
D
Serf2 +/+ +/+ +/- +/- -/- -/-
15
55
35
α-SERF2
α-beta-Actin
E
Body length (cm)
E15.5
E17.5
P0
F
Serf2+/+
Serf2-/-
G
Saccular space (%)
+/+
-/-

998

Figure 2

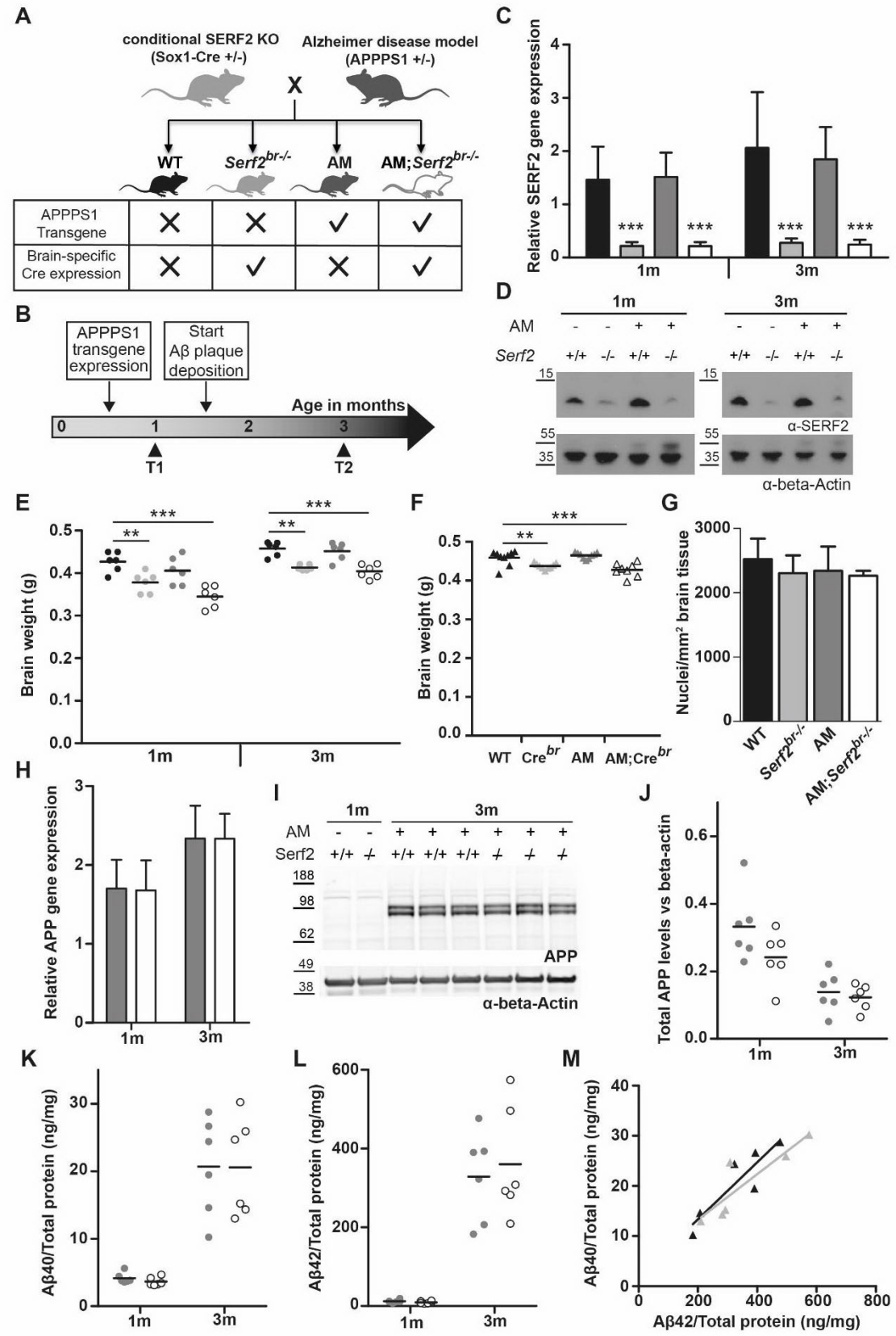
A
conditional SERF2 KO (Sox1-Cre +/-)
Alzheimer disease model (APPPS1 +/-)
X
WT
Serf2br-/-
AM
AM;Serf2br-/-
APPPS1 Transgene
Brain-specific Cre expression
B
APPPS1 transgene expression
Start Aβ plaque deposition
Age in months
T1
T2
C
Relative SERF2 gene expression
1m
3m
D
AM
Serf2
α-SERF2
α-beta-Actin
E
Brain weight (g)
F
Brain weight (g)
WT
Crebr
AM
AM;Crebr
G
Nuclei/mm² brain tissue
H
Relative APP gene expression
I
APP
α-beta-Actin
J
Total APP levels vs beta-actin
K
Aβ40/Total protein (ng/mg)
L
Aβ42/Total protein (ng/mg)
M
Aβ40/Total protein (ng/mg)
Aβ42/Total protein (ng/mg)

Figure 3

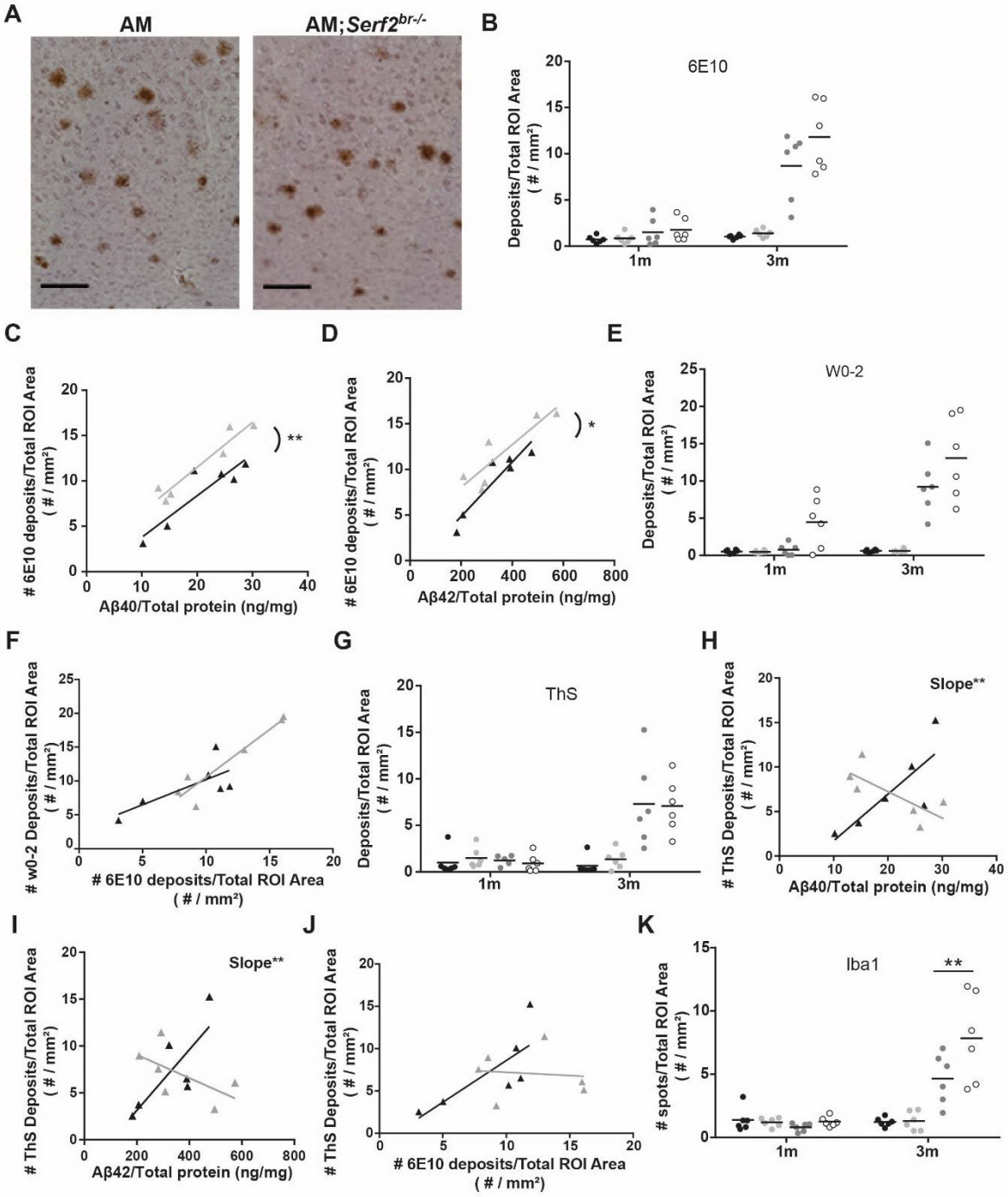
A
AM
AM;Serf2br-/-
B
6E10
Deposits/Total ROI Area (# / mm²)
1m
3m
C
6E10 deposits/Total ROI Area (# / mm²)
Aβ40/Total protein (ng/mg)
**
D
6E10 deposits/Total ROI Area (# / mm²)
Aβ42/Total protein (ng/mg)
*
E
W0-2
Deposits/Total ROI Area (# / mm²)
1m
3m
F
w0-2 Deposits/Total ROI Area (# / mm²)
6E10 deposits/Total ROI Area (# / mm²)
G
ThS
Deposits/Total ROI Area (# / mm²)
1m
3m
H
Slope**
ThS Deposits/Total ROI Area (# / mm²)
Aβ40/Total protein (ng/mg)
I
Slope**
ThS Deposits/Total ROI Area (# / mm²)
Aβ42/Total protein (ng/mg)
J
ThS Deposits/Total ROI Area (# / mm²)
6E10 deposits/Total ROI Area (# / mm²)
K
Iba1
**
spots/Total ROI Area (# / mm²)
1m
3m

Figure 4

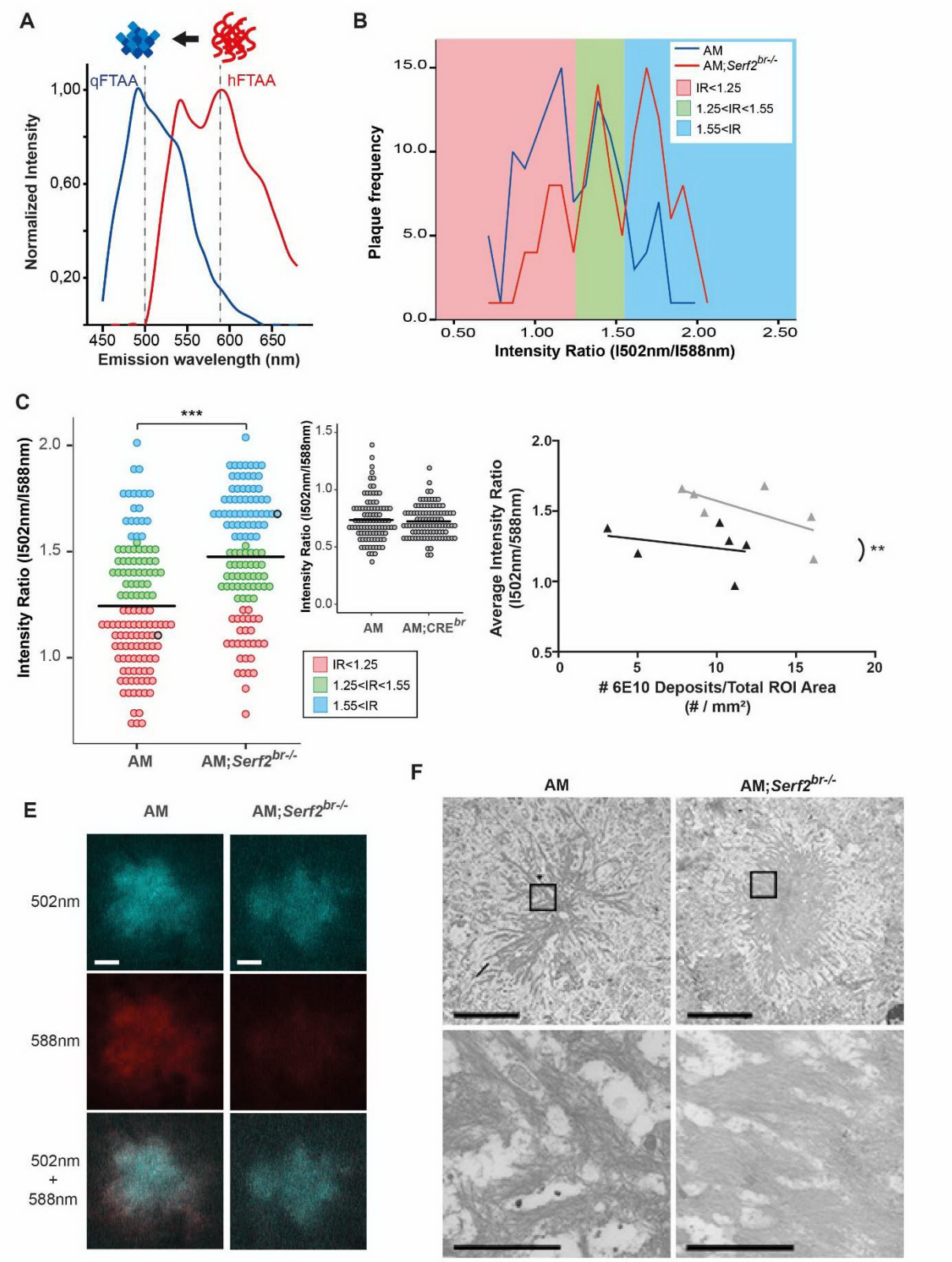
A
qFTAA
hFTAA
Normalized Intensity
1,00
0,60
0,20
450 500 550 600 650
Emission wavelength (nm)
B
AM
AM;Serf2br-/-
IR<1.25
1.25<IR<1.55
1.55<IR
Plaque frequency
15.0
10.0
5.0
0.0
0.50 1.00 1.50 2.00 2.50
Intensity Ratio (I502nm/I588nm)
C
***
Intensity Ratio (I502nm/I588nm)
2.0
1.5
1.0
AM
AM;Serf2br-/-
Intensity Ratio (I502nm/I588nm)
1.5
1.0
0.5
0.0
AM
AM;CREbr
IR<1.25
1.25<IR<1.55
1.55<IR
Average Intensity Ratio (I502nm/I588nm)
2.0
1.5
1.0
0.5
0 5 10 15 20
6E10 Deposits/Total ROI Area
(# / mm²)
**
E
AM
AM;Serf2br-/-
502nm
588nm
502nm
+
588nm
F
AM
AM;Serf2br-/-

998 **Supplemental figure legends**

999 **Supplemental Figure 1. Additional full-body *Serf2*$^{-/-}$ mice validation and phenotype**
1000 **confirmation. (A)** Targeting strategy used to delete exon 2 of *Serf2* by using the 'knockout-first'-
1001 allele (adjusted from Skarnes et al. 2011). Top panel: exon/intron structure of *Serf2* including the
1002 positions of the LacZ and Neo cassettes, as well as loxP sites. Bottom panel: the *Serf2* allele after
1003 recombination events as a result of crosses with *Hprt-Cre* mice. **(B)** Western blot analysis of liver,
1004 heart and brain tissue of a *Serf2*$^{+/+}$, *Serf2*$^{+/-}$ and *Serf2*$^{-/-}$ adult mice to detect Serf2 and actin. **(C)** Real
1005 time RT-PCR analyses of *Serf2* in different organs of adult mice with the following genotypes *Serf2*$^{+/+}$
1006 (n=3), *Serf2*$^{+/-}$ (n=8) and *Serf2*$^{-/-}$ (n=1). *Serf2* levels were normalized to the housekeeping gene 18S
1007 (mean ± SEM). **(D)** Lateral view of a *Serf2*$^{-/-}$ and *Serf2*$^{+/-}$ embryo and placenta at embryonic day 15.5
1008 and 17.5. **(E)** Weight measurements of *Serf2*$^{+/+}$, *Serf2*$^{+/-}$, *Serf2*$^{-/-}$ embryos at E17.5 and P0 (black line =
1009 mean, Two-way ANOVA with factors age and genotype, Bonferroni corrected post-hoc comparison
1010 for *Serf2*$^{+/-}$ and *Serf2*$^{-/-}$ compared to *Serf2*$^{-/-}$ *p<0.05; ***p<0.001). **(F)** Hematoxylin and Eosin staining
1011 on *Serf2*$^{-/-}$ and *Serf2*$^{+/+}$ lung and kidney tissue at E17.5 (10 times magnification). For all panels:
1012 *Serf2*$^{+/+}$= black, *Serf2*$^{+/-}$ = dark grey, *Serf2*$^{-/-}$ = light grey.

1013 **Supplemental Figure 2. Cell culture data of *Serf2* KO and control HEK cells and RNA**
1014 **sequencing analysis of mouse embryonic fibroblasts (MEFs) isolated from full-body *Serf2*$^{-/-}$ and**
1015 **control mice. (A)** Growth curve of two CRISPR-induced *Serf2*$^{-/-}$ clones of HEK293T versus wild-type
1016 HEK293T. (Three replicates measured,full line=replicate average, dashed lines=standard deviation on
1017 average) **(B)** Network showing the interconnectivity of enriched GO-terms in RNA sequencing data
1018 from *Serf2*$^{-/-}$ and control MEFs. Circle size indicates amount of differentially expressed genes found in
1019 each GO-category. Edges were drawn when the minor category shared more than 25 % of its found
1020 genes with the major category. Edge color indicates the major category in the relationship. Edge
1021 thickness indicates the percentage of found genes shared by the minor category. **(C)** Bar chart
1022 indicating the fold change for each GO-term as determined by DAVID. Brackets indicate the three
1023 main GO-term clusters defined based on the network in (B).

1024 **Supplemental Figure 3. Additional validation of the brain-specific knock-out of *Serf2*. (A)**
1025 Modified targeting strategy used to delete the exon 2 of *Serf2* specifically in the central nervous
1026 system. **(B)** Real time RT-PCR analyses of *Serf2* RNA expression in different organs *Serf2*$^{+/+}$ and
1027 *Serf2*$^{br-/-}$ female mice at 1 month and 3 months of age. *Serf2* expression was normalized to
1028 housekeeping gene beta-actin (all groups n=6, mean ± SEM). **(C)** Western blot analysis and
1029 quantification of *Serf2* and beta-actin in brain lysates of WT and *Serf2*$^{br-/-}$ female mice at 1 month
1030 (both groups n=6, mean ± SEM, t-test **p<0.01). **(D)** Brain weight of unfloxed WT and CRE^{br} mice at
1031 1 and 3 months of age (black line = mean, Two-way ANOVA with factors age and genotype,
1032 Bonferroni corrected post-hoc for CRE^{br} compared to WT *p_{bon}<0.05). **(E)** Evolution of brain weight
1033 in WT and *Serf2*$^{br-/-}$ female mice between 1 and 11 months of age (black line = mean).

1034 **Supplemental Figure 4. Overview of distribution and general morphological parameters of**
1035 **6E10-stained Aβ deposits in AM and AM;*Serf2*$^{br-/-}$ mice at 3 months of age. (A)** Light microscope
1036 images of the 6E10 immunostained sagittal section of 3-month-old AM and AM;*Serf2*$^{br-/-}$ female mice
1037 (scale bar = 1mm, black rectangle = magnified region in main Figure 3). **(B)** Boxplots showing the
1038 distribution of the surface area of the individual plaques measured in AM and AM;*Serf2*$^{br-/-}$ mice at 3
1039 months of age. **(C)** Boxplots showing the distribution of the circularity of the individual plaques
1040 measured in AM and AM;*Serf2*$^{br-/-}$ mice at 3 months of age. **(D)** Boxplots showing the distribution of
1041 the solidity of the individual plaques measured in AM and AM;*Serf2*$^{br-/-}$ mice at 3 months of age. For
1042 all boxplots: black line = median, box = 25th-75th percentile, whiskers = 1.5 x interquartile range
1043 (IQR), circles = outlier value > 1.5x IQR, asterisks = extreme outlier value > 3x IQR.

1044 **Supplemental Figure 5. Overview of distribution and detailed W0-2-stained Aβ deposits in AM**
1045 **and AM;*Serf2*$^{br-/-}$ mice at 3 months of age.** Light microscope images of the W0-2 immunostained
1046 sagittal section of 3-month-old AM and AM;*Serf2*$^{br-/-}$ female mice (scale bar = 1mm, black rectangle =
1047 magnified in insert on the right, insert scale bar = 100µm).

1048 **Supplemental Figure 6. Correlation plots illustrating the relationship of different stains in**
1049 **individual mice. (A)** Correlation plot depicting the relationship between the density of 6E10 deposits

1050 and Iba1-positive spots in AM (black) and AM;*Serf2*$^{br-/-}$ (grey) mice at 3 months of age. **(B)**
1051 Correlation plot depicting the relationship between W0-2 plaque density and the LCO average
1052 intensity ratio in AM (black) and AM;*Serf2*$^{br-/-}$ (grey) mice at 3 months of age. **(C)** Correlation plot
1053 depicting the relationship between ThS plaque density and the LCO average intensity ratio in AM
1054 (black) and AM;*Serf2*$^{br-/-}$ (grey) mice at 3 months of age. For all plots: detailed statistics in
1055 Supplemental Table 3; *p <0.05.

1056 **Supplemental Figure 7. Overview and detailed view of Aβ staining pattern after W0-2 and 6E10**
1057 **staining in AM and AM;*Serf2*$^{br-/-}$ mice at 1 month of age. (A)** Light microscope images of the W0-2
1058 immunostained sagittal section of 1-month-old AM and AM;*Serf2*$^{br-/-}$ female mice. **(B)** Light
1059 microscope images of the 6E10 immunostained sagittal section of 1-month-old AM and AM;*Serf2*$^{br-/-}$
1060 female mice. All pictures: main scale bar = 1mm, black rectangle = magnified in insert on the right,
1061 insert scale bar = 100µm.